

Prospects for Detecting Gaps in Globular Cluster Stellar Streams in External Galaxies with the Nancy Grace Roman Space Telescope

CHRISTIAN AGANZE,¹ SARAH PEARSON,^{2,*} TJITSKE STARKENBURG,³ GABRIELLA CONTARDO,⁴ KATHRYN V. JOHNSTON,^{5,6}
KIYAN TAVANGAR,⁶ ADRIAN M. PRICE-WHELAN,⁵ AND ADAM J. BURGASSER^{1,7}

¹Center for Astrophysics and Space Sciences (CASS), University of California, San Diego, La Jolla, CA, 92093, USA

²Center for Cosmology and Particle Physics, Department of Physics, New York University, 726 Broadway, New York, NY 10003, USA

³Center for Interdisciplinary Exploration and Research in Astrophysics (CIERA), Northwestern University, 1800 Sherman Ave, Evanston IL 60201, USA

⁴International School for Advanced Studies (SISSA), Via Bonomea, 265, 34136 Trieste TS, Italy

⁵Center for Computational Astrophysics, Flatiron Institute, 162 Fifth Avenue, New York, NY 10010, USA

⁶Department of Astronomy, Columbia University, 550 West 120th Street, New York, NY, 10027, U.S.

⁷Department of Astronomy and Astrophysics, University of California, San Diego, La Jolla, CA, 92093, USA

(Received receipt date; Accepted acceptance date)

ABSTRACT

Stellar streams form through the tidal disruption of satellite galaxies or globular clusters orbiting a host galaxy. Globular cluster streams are of particular interest since they are thin (dynamically cold) and therefore sensitive to perturbations from low-mass subhalos. Since the subhalo mass function differs depending on the dark matter composition, these gaps can provide unique constraints on dark matter models. However, current samples are limited to the Milky Way. With its large field of view, deep imaging sensitivity, and high angular resolution, the upcoming *Nancy Grace Roman Space Telescope* (*Roman*); presents a unique opportunity to significantly increase the number of observed streams and gaps. This paper presents a first exploration of the prospects for detecting gaps in streams in M31 and other nearby galaxies with resolved stars. We simulate the formation of gaps in a Palomar-5-like stream and generate mock observations of these gaps together with background stars in M31 and foreground Milky Way stellar fields. We assess *Roman*'s ability to detect gaps out to 10 Mpc through visual inspection and with the gap-finding tool `FindTheGap`. We conclude that gaps of ≈ 1.5 kpc in streams that are created from subhalos of masses $\geq 5 \times 10^6 M_\odot$ are detectable within a 2–3 Mpc volume in exposures of 1000s–1 hour. This volume contains ≈ 200 galaxies. Large samples of stream gaps in external galaxies will open up a new era of statistical analyses of gap characteristics in stellar streams and help constrain dark matter models.

1. INTRODUCTION

Large-scale cosmological simulations with cold dark matter (Λ CDM) predict hierarchical formation of dark matter halos and the existence of substructure at all scales (White & Rees 1978; Blumenthal et al. 1984; Bullock et al. 2001; Springel et al. 2008; Fiacconi et al. 2016). To test Λ CDM predictions at small scales, previous studies have uncovered satellite galaxies around the Milky Way and dwarf galaxies in the local group with stellar masses down to $10^3 M_\odot$ (Willman et al. 2005; Simon & Geha 2007; Martin et al. 2008; Koposov et al. 2009; Willman et al. 2011; McConnachie 2012; Bechtol et al. 2015; Drlica-Wagner et al. 2015; Geha et al.

2017; Mao et al. 2021). However, in Λ CDM models, galaxies with halos of masses $\lesssim 10^8 M_\odot$ are more dominated by dark matter compared to higher-mass galaxies, which makes their detection difficult (Efstathiou 1992; Okamoto et al. 2008; Bullock et al. 2000; Sawala et al. 2016). Other dark matter models differ from Λ CDM in their predictions for the masses and number densities of dark matter subhalos (subhalo mass functions). For instance, warm dark matter models (WDM, Bode et al. 2001) predict a similar hierarchical collapse at large scales, but this collapse is strongly suppressed at lower masses ($\lesssim 10^9 M_\odot$, depending on particle mass), resulting in a smaller fraction of low-mass subhalos (Bose et al. 2017). Similarly, some fuzzy cold dark matter models (Hu et al. 2000; Hui et al. 2017), predict a sharp cutoff at low masses ($\leq 10^7 M_\odot$). Self-interacting dark

* NASA Hubble Fellow

matter (SIDM) models produce halos with pronounced cores with different tidal evolution, masses and densities compared to CDM halos (Spergel & Steinhardt 2000; Rocha et al. 2013; Tulin & Yu 2018; Glennon et al. 2022; Forouhar Moreno et al. 2022). Even in Λ CDM simulations, the survival and the properties of low-mass subhalos within a larger halo are poorly understood. The tidal field of the central galaxy, pre-existing substructure in the halo, and deviations from a smooth spherical halo density profile can all affect the tidal evolution of accreted subhalos (Garrison-Kimmel et al. 2017). On the other hand, analytical calculations, N-body simulations and high-resolution hydrodynamical simulations show that the central cores of subhalos are likely to survive for long periods of time, or even indefinitely (van den Bosch et al. 2018; van den Bosch & Ogiya 2018; Errani & Peñarrubia 2020).

All of these differences between different dark matter models can, in principle, be tested by statistical surveys of nearby low-mass subhalos. The key challenge is how to detect these invisible dark subhalos. Strong gravitational lensing offers an opportunity to validate predictions of dark matter models (Dalal & Kochanek 2002; Amara et al. 2006; Nierenberg et al. 2014; Hezaveh et al. 2016; Nierenberg et al. 2017; Gilman et al. 2019). However, this technique probes all subhalos along the line of sight up to the lensed luminous source, which complicates the inference of dark matter properties.

Globular cluster (GC) streams provide a complementary approach for detecting and measuring the spectrum of low-mass subhalos in the local volume (Johnston et al. 2002; Yoon et al. 2011; Bovy 2016; Bovy et al. 2017). As GCs orbit the host galaxy, internal evolution and tidal stripping leads to the escape of stars from the central cluster, forming thin, elongated stellar streams which persist for billions of years (Johnston 1998; Helmi & White 1999). These streams can subsequently be perturbed by a free-floating dark matter subhalo, which can create a gap-like feature inside the stream (Yoon et al. 2011). Numerical and analytical calculations predict the morphology and frequency of these features in various types of GC streams (Yoon et al. 2011; Carlberg 2012; Erkal et al. 2016; Sanderson et al. 2016; Koppelman & Helmi 2021).

Photometric and spectroscopic surveys have identified and characterized ≈ 100 stellar streams in the Milky Way, with the majority being globular cluster streams (Odenkirchen et al. 2001; Newberg et al. 2002; Majewski et al. 2003; Odenkirchen et al. 2009; Newberg et al. 2009; Grillmair & Carlin 2016; Shipp et al. 2018; Mateu et al. 2018; Ibata et al. 2019; Li et al. 2022; Martin et al. 2022; Mateu 2023). A few of these GC streams show evidence

of gap-like features that are predicted in numerical simulations of dark matter subhalo encounters (de Boer et al. 2018, 2020; Bonaca et al. 2020; Tavangar et al. 2022). In particular, Price-Whelan & Bonaca (2018) identified a spur and a gap in GD-1, which Bonaca et al. (2019) attributed to a likely encounter with a 10^6 – 10^7 dark matter subhalo ~ 8 Gyr ago, after ruling out other types of perturbers.

Gaps in GC streams can be created through other processes, however. Previous studies have shown that baryonic matter perturbers (galactic bars, molecular clouds, black holes, spiral arms) can create similar features in GC streams (Amorisco et al. 2016; Hattori et al. 2016; Price-Whelan et al. 2016; Erkal et al. 2017; Pearson et al. 2017; Banik & Bovy 2019; Bonaca et al. 2020), which makes gaps difficult to decipher, even when they are detected. Moreover, since these streams have intrinsically low surface brightnesses, the detection of gaps has been limited to the Milky Way, which has resulted in relatively small samples.

Detecting gaps in globular cluster streams in external galaxies offers a new window into testing dark matter models by increasing the number and diversity of stream gaps. Previous studies have observed streams in external galaxies arising from tidally-disrupted satellites (Martínez-Delgado et al. 2010; Martínez-Delgado et al. 2021). While several candidate GC streams have been proposed in M31 (Pearson et al. 2022), these candidate detections require more sensitive and higher resolution data to be confirmed, and to eventually map both the streams and gap structures.

The upcoming *Nancy Grace Roman Space Telescope* (Spergel et al. 2015) will have a large field of view, high angular resolution and deep-imaging sensitivity. Pearson et al. (2019, 2022) demonstrated how this combination allows the detection of very low-surface brightness GC streams out to a couple of Mpc. In this work, we examine the plausibility of detecting gaps in Pal 5-like GCs formed from interactions with dark matter subhalos by extending the predictions of Pearson et al. (2019). The paper is arranged as follows: Section 2 describes our methodology for simulating isolated, evolving streams with gaps; Section 3 discusses our simulations of mock observations with *Roman* including foreground and background star fields; and the feasibility of visual inspection to confirm gaps in simulated star count data. Section 4 discusses the application of an automatic gap-finding pipeline, **FindTheGap** (Contardo et al. 2022), to find gaps in simulated data. Section 5 discusses the implications and limitations of this work. We summarize our findings in Section 6.

2. SIMULATING GLOBULAR CLUSTER STREAMS WITH GAPS

Our goal is to simulate observations of gaps in GC streams, starting with the Palomar 5 stream (hereafter, Pal 5; Odenkirchen et al. 2001, 2003) as a test case, defined to have a present-day mass of $10^4 M_\odot$ (Ibata et al. 2017). Our work closely followed a similar methodology as Pearson et al. (2019), with additional modifications that are described herein. We conducted all numerical calculations with the `gala` package (Price-Whelan 2017), which implements numerical integration techniques to model the orbits of stars in a pre-specified static potential.

2.1. Gravitational Potentials

In our analysis, we used M31 as the external host galaxy. Many groups have estimated the total mass and the potential of M31 by modeling the kinematics of satellites (Watkins et al. 2010); constraining the rotation curve (Chemin et al. 2009); modeling the velocity distributions using tracer particles such as stars, globular clusters, and planetary nebulae (Kaffe et al. 2018); dynamical modeling of the giant southern stream (GSS) in M31 (Fardal et al. 2013); and the local group timing argument (González et al. 2014; Chamberlain et al. 2022). Additional references and trade-offs from these techniques are summarized by Fardal et al. (2013) and Kaffe et al. (2018).

To set up an M31-like potential, we used the model by Kaffe et al. (2018) composed of a central bulge, a disk, and a halo. The bulge potential follows a Hernquist profile (Hernquist 1990) given by:

$$\Phi_b(r) = -\frac{GM_b}{r+q} \quad (1)$$

with a scale length (q) of 0.7 kpc and a bulge mass (M_b) of $3.4 \times 10^{10} M_\odot$. The disk potential follows a Miyamoto-Nagai density profile (Miyamoto & Nagai 1975) given by:

$$\Phi_d(R, z) = -\frac{GM_d}{\left(R^2 + \left(a + (z^2 + b^2)^{\frac{1}{2}}\right)^2\right)^{1/2}} \quad (2)$$

with a scale length (a) of 6.5 kpc, a scale height (b) of 0.26 kpc and a total disk mass (M_d) of $6.9 \times 10^{10} M_\odot$. These parameters for the disk and the bulge were adopted from a compilation of literature values (Bekki et al. 2001; Font et al. 2006; Geehan et al. 2006; Seigar et al. 2008; Chemin et al. 2009; Corbelli et al. 2010; Tamm et al. 2012). We assumed a Navarro-Frenk-White (NFW) profile (Navarro et al. 1996) for the halo given

by:

$$\Phi_h(r) = -\frac{G M_{vir} \ln(1+r c/r_{vir})}{g(c) r}, \quad (3)$$

$$\text{with } g(c) = \ln(1+c) - c/(1+c), \quad (4)$$

$$M_{vir} = \frac{4\pi}{3} r_{vir}^3 \Delta \rho_c, \quad (5)$$

$$\text{and } \rho_c = \frac{3H_0^2}{8\pi G} \quad (6)$$

Where M_{vir} is the virial mass, r_{vir} is the virial radius, c is the concentration parameter, Δ is the virial overdensity parameter and ρ_c is the critical density of the universe. As many of these parameters are interrelated, we used best-fit values for the halo virial mass at $\Delta = 200$ of $M_{200} = 0.7 \times 10^{12} M_\odot$, and $\log c = 1.5$ based on the inferred posterior distribution by Kaffe et al. (2018). We note that the concentration parameter was poorly constrained in this work. We also assumed $H_0 = 67.7$ km/(Mpc s) based on Planck results (Planck Collaboration et al. 2020).

For the dark matter subhalo, we again assumed a Hernquist density profile with masses (M_h) and radii (r_h) determined by the scaling relation from Erkal et al. (2016):

$$r_h = 1005 \text{ pc} \times \left(\frac{M_h}{10^8 M_\odot}\right)^{0.5}. \quad (7)$$

2.2. Stream Progenitor Coordinates

As there are no currently-known globular cluster streams in M31, we used a Pal 5-like stream as an example. In the Milky Way, the Cartesian Galactocentric coordinates of Pal 5 are $(X, Y, Z) = (6.1 \text{ kpc}, 0.2 \text{ kpc}, 14.7 \text{ kpc})$ and $(V_X, V_Y, V_Z) = (-49.7 \text{ km/s}, -119.4 \text{ km/s}, -11.4 \text{ km/s})$ (Price-Whelan et al. 2019; Vasiliev 2019)¹. Our goal is to test the observability of gaps in streams located at various locations in galactic halos, hence, we also simulated streams to galactocentric radii of 35 kpc and 55 kpc. For simplicity, to simulate equivalent streams at 35 kpc and 55 kpc, we used positions that give approximately the desired Galactocentric radii, and we assumed that the velocities of the stream at 35 kpc and 55 kpc were the same as the velocity at 15 kpc. We used the same velocities (V_X, V_Y, V_Z) for all streams, but we note that

¹ We assumed that our GC progenitor lies at the present-day heliocentric equatorial coordinates of Pal 5, $(\alpha, \delta) = (229^\circ 022, -0^\circ 112)$ at a distance of 22.5 kpc; and has a proper motion vector $(\mu_\alpha \cos \delta, \mu_\delta) = (-2.736 \text{ mas/yr}, -2.646 \text{ mas/yr})$ and radial velocity of -58.60 km/s . We assumed a galactocentric coordinate system with the local standard of rest velocity $\vec{V}_{lsr} = (8.4 \text{ km/s}, 251.8 \text{ km/s}, 8.4 \text{ km/s})$ and the Sun radial distance of 8.275 kpc from the Galactic center based on (Schönrich et al. 2010; Bovy et al. 2012; GRAVITY Collaboration et al. 2019).

this process results in different orbits compared to the stream at 15 kpc. These coordinates, along with additional parameters of our simulations are all summarized in Tables 1 and 2.

2.3. Generating a Gap in the Stream

We generated model streams using the “particle-spray” method described by Fardal et al. (2015) and implemented in `gala`. We assumed a uniform mass loss history and a progenitor mass (m_p) of $5 \times 10^4 M_\odot$ based on Bonaca et al. (2020). We simulated the direct impact of a dark matter subhalo and a stream using `gala`; specifically, the function `MockStreamGenerator` which models the orbits of stars influenced by a massive body within an external potential. Throughout these calculations, individual stream stars were treated as non-interacting massless particles, and we did not include the stream’s progenitor potential.

To ensure a direct impact between stream and subhalo, we first needed to determine the initial coordinates of both components given their positions and velocities at the moment of collision. We backward-integrated the present-day coordinates of the stream progenitor to a time t_1 , initiated a stream at these coordinates, and then forward-integrated by Δt_2 . At this point, the collision position was assumed to be at a position Δx away from the progenitor position. We adjusted the coordinates of the subhalo to achieve a fixed relative velocity ($|\vec{V}_{\text{rel}}|$) between the stream stars and the subhalo perpendicular to the impact location. After we determined the position and velocity of the subhalo at the collision point, we backward-integrated its orbit by Δt_2 again to set the subhalo’s initial conditions.

With the initial positions and velocities of the stream and subhalo determined, we forward-integrated the system for Δt_2 , computing the stream particle/subhalo interaction using the `gala DirectNBody` routine, with an additional Δt_3 time period to allow the subhalo to pass completely through the stream. At this point, we removed the subhalo from the simulation to avoid potential multiple interactions, allowing for a more direct analysis of the observability of well-defined gaps in streams. We then forward-integrated the stream stars for the remaining $t_1 - (\Delta t_2 + \Delta t_3)$ to observe the growth of the gap over time.

These timescales (t_1 , Δt_2 and Δt_3) were chosen to allow the stream to have similar lengths as that of Pal 5 in M31 (7–12 kpc at $R_{GC}=15$ –55 kpc, based on estimates by Pearson et al. 2019). Additionally, after the subhalo encounter, we continued releasing stars into the mock stream to ensure that there isn’t a gap at the location of the progenitor. We later re-sampled the stream

to match the number of stars observed in Pal 5 in the Milky Way based on Bonaca et al. (2020). Table 2 summarizes all parameters for streams at 15 kpc, 35 kpc and 55 kpc.

2.4. Quantifying the Size of the Simulated Gap

To estimate the size of the simulated gap, we fit a Gaussian near the visually-identifiable gap. To account for the density variation along the stream and the decrease in density near the wings of the stream, we measured both the density ratio and the density difference between the perturbed stream (with a gap) and an equivalent unperturbed stream. By averaging the full width at half maximum of the Gaussian fits to both the density ratios and density difference, we obtained gap sizes of 1.4 kpc, 1.8 kpc, and 1.8 kpc, at $R_{GC}=15$ kpc, 35 kpc and 55 kpc, respectively for subhalo masses of $5 \times 10^6 M_\odot$. We note that in our stream integration procedure, the orbits of the stream and the subhalo, the total integration times, and the impact velocities were chosen to achieve the desired lengths (7–12 kpc) of the stream and to obtain approximately the same gap sizes at all galactocentric values.

Figure 1 depicts three simulated Pal 5-like streams at $R_{GC}=15$ kpc with gaps induced by dark matter subhalos with masses of $2 \times 10^6 M_\odot$, $5 \times 10^6 M_\odot$, and $10^7 M_\odot$. The size of the gap increases with the mass of the subhalo, as previously shown by analytical and numerical simulations (Yoon et al. 2011; Erkal & Belokurov 2015). Our results are consistent with numerical simulations by Yoon et al. (2011), who found that gaps induced by 10^5 – $10^{7.5} M_\odot$ subhalos can be visually identified in Pal 5-like streams, although they used a higher relative impact velocity (>100 km/s), a single galactocentric radius ($R_{GC} \approx 25$ kpc) and a longer integration times after the impact (≈ 4.34 Gyr). In their simulations, they found that subhalo masses $\geq 10^6 M_\odot$ induce gaps with physical sizes of ≈ 1 kpc (visually), comparable to the observed gaps in our simulations. However, we note that even when using similar impact parameters and integration times, centrally-concentrated halo profiles (e.g NFW profiles) will result in larger gaps (Sanders et al. 2016).

3. GENERATING MOCK OBSERVATIONS OF STREAMS WITH GAPS IN M31 AND OTHER EXTERNAL GALAXIES

In order to model the observability of both streams and gaps, we need to generate mock observations of our

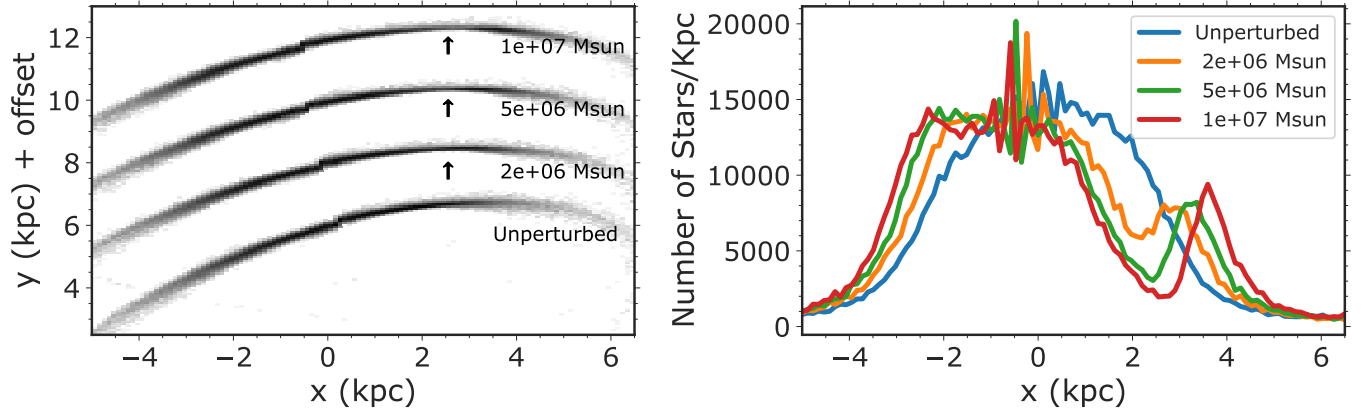


Figure 1. Results from our simulations of a gap in a stream at $R_{GC}=15$ kpc. The total number of stars in each stream is $\approx 80,000$ and the mass of the stream is $50,000 M_{\odot}$. *Left*: Gaps are induced by collisions with dark matter subhalos of masses of $2 - 10 \times 10^6 M_{\odot}$. Each stream is offset by a constant displacement in the y-direction for display purposes and the relative velocity between the stream stars and the subhalo is 50 km/s. For comparison, we show an unperturbed stream of the same mass and trajectory. Arrows indicate the location of the gap, and we label the mass of the perturber. *Right*: Linear density of stars along the x-direction in each stream. In both plots, under-densities in perturbed streams can be identified by eye for subhalos with masses $\geq 2 \times 10^6 M_{\odot}$.

Table 1. Summary of simulation parameters for the stream and the subhalo

	Parameter	Description	Range of Values
Stream	m_p	progenitor mass	$5 \times 10^4 M_{\odot}$
	–	number of particles	$\approx 80,000$
Subhalo	M_h	mass	$2 \times 10^6 M_{\odot} - 10^7 M_{\odot}$
	r_s	scale radius	0.14 kpc–0.32 kpc
	–	potential	Hernquist ^a
Galaxy	–	potential	Hernquist bulge + Miyamoto-Nagai disk + NFW halo ^b

^aHernquist (1990).

^b Profiles based on Miyamoto & Nagai (1975) and Navarro et al. (1996) with parameters based on Milky Way measurements by McMillan (2017).

streams in external galaxies as they will appear with *Roman*, by taking into account sensitivity, resolution, and contamination from Milky Way foreground and the host galaxy halo background stellar populations. To address contaminant populations, we followed a method similar to Pearson et al. (2019) as applied to observations of the halo of M31. In these simulations, we assumed all stars are resolved down to our assumed magnitude limits.

3.1. Simulating Mock Observations with Roman

We obtained M31 data from the Pan-Andromeda Archaeological Survey (PAndAS, McConnachie et al. 2009;

Martin et al. 2016; McConnachie et al. 2018, Ibata et al., private communication). The PAndAS survey provides wide-field imaging data for the Milky Way, M31 and other nearby galaxies over a total area of 300 deg^2 , with the 3.6-meter Canada-France-Hawaii Telescope (CFHT) MegaPrime/MegaCam camera in the optical and infrared u , g , r , i , and z filters. We used extinction-corrected CFHT AB magnitudes (denoted by g_0 and i_0) based on the corrections by Ibata et al. (2014). We selected three patches with projected areas of $10 \text{ kpc} \times 10 \text{ kpc}$ at the distance of M31 at radial separations of 15 kpc, 35 kpc, and 55 kpc from its

Table 2. Summary of the stream, subhalo coordinates and resulting gap sizes

Parameter and Description		R _{GC} = 15 kpc	R _{GC} = 35 kpc	R _{GC} = 55 kpc
initial	progenitor position at t ₁ (\vec{x}_1 , kpc)	(6.1, 0.2, 14.7)	(6.1, 0.2, 34.7)	(6.1, 31.7, 44.7)
	progenitor velocity at t ₁ (\vec{v}_1 , km/s)	(-49.7, -119.4, -11.4)	(-49.7, -119.4, -11.4)	(-49.7, -119.4, -11.4)
	total integration time (t ₁ , Gyr)	2	3	3
collision	$ \vec{V}_{\text{rel}} $, km/s	50	70	50
	time before collision (Δt_2 , Gyr)	0.7	1.7	1.5
	time during collision (Δt_3 , Gyr)	0.5	0.5	0.1
	distance of impact from center (Δx , kpc)	0.5	0.7	0.8
result	size of the gap (kpc)	1.4	1.8	1.8

center, corresponding to regions of ≈ 0.5 deg² on the sky. To generate mock *Roman* observations, we assumed a total field of view of 0.28 deg² (not simulating the shape of the detector) and limiting Vega magnitudes of $Z(F087) = 27.15$ for 1000s exposures and $Z(F087) = 28.69$ for 1-hour exposures.² As in [Pearson et al. \(2019\)](#), we limited our analysis to $R(F062)$ and $Z(F087)$ bands.

3.1.1. Simulating Milky Way Foregrounds

We simulated foregrounds along the line of sight of M31 assuming a central coordinate of R.A. = 0.57 deg and decl. = 43.1 deg based on the central coordinates of the M31 PAndAS field. We used a Kroupa power-law initial mass function (IMF) ([Kroupa 2001](#)) for stellar masses between 0.1 M_⊙ and 120 M_⊙, isochrones from the PAdova and tRieste Stellar Evolution Code ([Bressan et al. 2012](#), PARSEC) spanning ages of 4 Myr-13 Gyr, and metallicities $-2.0 \leq [\text{Fe}/\text{H}] \leq 0.2$ that realistically encompass the Milky Way thin and thick disks and halo populations. We sampled 10⁶ stars with masses from the IMF, assigned ages and metallicities based on uniform distributions, and computed CFHT g_0 and i_0 and *Roman* R and Z absolute magnitudes by interpolating in initial mass–absolute magnitude space for every combination of metallicity and age.

We assigned distances drawn from a galactic density model composed of a thin disk, thick disk, and a halo based on [Jurić et al. \(2008\)](#). The total stellar density is given by:

$$\rho = \rho_{\text{thin disk}} + f_0 \times \rho_{\text{thick disk}} + f_1 \times \rho_{\text{halo}}, \quad (8)$$

where f_0 and f_1 are the relative fraction of thick disk and halo stars to the thin disk population at the position of the Sun, set to 0.12 and 0.005 respectively. Stellar

densities for the disk were assumed to follow exponential profiles parameterized by a scale height (H) and scale length (L):

$$\rho_{\text{disk}} = \rho_{\odot} \exp\left(-\frac{R - R_{\odot}}{L}\right) \exp\left(-\frac{|z - Z_{\odot}|}{H}\right) \quad (9)$$

For the thin disk, we assumed $H = 300$ pc and $L = 2600$ pc. For the thick disk, we assumed $H = 900$ pc and $L = 3600$ pc. We also assumed $R_{\odot} = 8.3$ kpc and $Z_{\odot} = 0.027$ kpc ([Jurić et al. 2008](#)). While the scale height of a population varies with its main-sequence lifetime ([Bovy 2017](#)), and dynamical evolution leads to asymmetries in the density profile ([Reylé et al. 2009](#); [Liu et al. 2017](#); [Nitschai et al. 2021](#)), these simple assumptions provide a reasonable first-order estimate of the broad stellar densities of present-day Milky Way stellar populations. For the halo stellar density, we used a flattened spheroid profile:

$$\rho_{\text{halo}} = \left(\frac{R_{\odot}}{(R^2 + (z/q)^2)^{\frac{1}{2}}}\right)^n \quad (10)$$

with $q = 0.64$ and $n = 2.77$. We drew distances from a probability distribution function $P(d) = d^2 \times \rho(R, z)$ out to 100 kpc.

After we estimated the distance distribution of Milky Way stars, we computed their observable apparent magnitudes. To model the magnitude uncertainty, we fit the magnitude dependence of the uncertainty (δmag) for CFHT g_0 and i_0 filters based on the [McConnachie et al. \(2018\)](#) point sources³. We then assigned apparent g_0 and i_0 magnitudes for the simulated population by drawing from a normal distribution with a scatter equal

² https://roman.ipac.caltech.edu/sims/Param_db.html

³ We selected point sources from the [McConnachie et al. \(2018\)](#) catalog by restricting the morphology flags in the g and i bands to -1. The catalog can be accessed at <https://www.cadc-ccda.hia-ihp.nrc-cnrc.gc.ca/en/community/pandas/query.html>

to the standard deviation of the estimated dependence. For all *Roman* magnitudes we assumed a constant uncertainty of 0.1 mag; but the true uncertainty will likely vary with magnitude and exposure time.

Finally, we determined the total number of stars that are observable by *Roman* at a given magnitude limit by scaling the simulated Milky Way foreground distribution to the observed PAndAS data within the region of the color-magnitude diagram bound by $2 < g_0 - i_0 < 3$ and $18 < i_0 < 21$. This region in the color-magnitude diagram is predominantly covered by Milky Way foreground isochrones, which makes it ideal for scaling our total number of foreground stars. We then applied the magnitude limit cut corresponding to 1 hour and 1000s exposure. While this scaling does not take into account exact selection effects, it provided a first-order estimate for the number of stars that can be observed by *Roman*. We obtained an agreement between our simulations and both the color-magnitude diagrams and the final g_0 -band luminosity function from the PAndAS data in Figure 2; and we further discuss limitations in our foreground and background simulations in Section 5.2.

3.1.2. Simulating Background Stars in M31 and Other External Galaxies

We selected PARSEC isochrone tracks that span ages of 5 Gyr to 13 Gyr and metallicities $-2.0 \leq [\text{Fe}/\text{H}] \leq +0.5$ to cover the approximate range of ages and metallicities of stars in the halo of M31 (Brown et al. 2003; Ibata et al. 2014). Similar to the Milky Way simulation, we assumed a Kroupa initial mass function for stellar masses between $0.1 M_\odot$ and $120 M_\odot$, a uniform age distribution, and a uniform metallicity distribution in chosen patches of $10 \text{ kpc} \times 10 \text{ kpc}$ at galactocentric radii (R_{GC}) of 15 kpc, 35 kpc and 55 kpc. The PAndAS survey and other previous studies have characterized the metallicity and abundance distributions (e.g. Escala et al. 2020) of small regions of M31’s stellar halo in detail. As our goal is to estimate stellar number densities, assuming a general set of old and metal-poor stellar populations in all regions of the stellar halo was deemed sufficient. Throughout, we assumed the distance to M31 to be 770 kpc (distance modulus of 24.4, Ibata et al. 2014).

To assign distances to stars in the halo of M31, we modeled the stellar density as a flattened spheroid profile based on Ibata et al. (2014). The 3D stellar density is given by:

$$\rho_{\text{M31}} = \left((\tilde{R}^2 + (\tilde{z}/q)^2)^{\frac{1}{2}} \right)^n \quad (11)$$

(cf. Eqn. 10), where \tilde{R} and \tilde{z} are the cylindrical radius and height starting from the center of M31, in the plane

and perpendicular to its disk respectively, with $q = 1.11$, and $n = -3$. We drew distances assuming that the halo of M31 extends to $\approx 100 \text{ kpc}$ (Chapman et al. 2006) and we assigned projected distances to M31 halo stars as $d = 770 \text{ kpc} + \tilde{z}$, where \tilde{z} is the randomly-drawn cylindrical galactocentric height for simplicity.

Finally, we assigned apparent magnitudes and magnitude uncertainties in a similar manner as for Milky Way foreground stars. To obtain the correct normalization for the number of stars, we scaled the total number of stars to the observed number between $0.5 < g_0 - i_0 < 2$ and $21.5 < i_0 < 23.5$ in the PAndAS data as there is a significant drop-off in the PAndAS magnitude completeness to below $\approx 70\%$ for $i_0, g_0 > 23.5$ (Martin et al. 2016). As a final check, we examined the simulated luminosity function (number of stars as a function of magnitude) in the CFHT g -band based on our CMD-based scaling, luminosity function inferred from PAndAS data.

Figure 2 the combined CHFT g – band luminosity function of both components (M31 population and the Milky Way foregrounds) compared to the observed luminosity function from the PAndAS data, and it shows the simulated *Roman* color-magnitude diagram. This illustrates that Milky Way foreground stellar populations are dominated by sources with $Z < 25$, while M31 includes stars with $Z > 20$. In real *Roman* observations, it will be possible to separate most Milky Way foreground stars from M31 stars based on their positions on the CMD ($R - Z$ vs Z space, see Figure 2). We note that low-mass stars and brown dwarfs are lacking in our simulated foregrounds, hence they may introduce an additional source of contamination in the real data. Nevertheless, we found a general agreement between the simulated and the observed luminosity function in the CFHT bands. We further show a comparison between our simulations and the PAndAS data in Appendix A. While the region corresponding to the Milky Way disk is reasonably well-matched, we could not reproduce all of the structures in the CFHT CMDs, perhaps due to an underestimation of the halo and thick disk fraction along this line of sight.

To further validate our methodology for simulating stellar populations, we compared our surface densities to the CFHT data and predictions of Pearson et al. (2019). For 1-hour exposure with *Roman*, we obtained stellar densities of $3.1 \times 10^5 \text{ stars/degrees}^2$ at $R_{\text{GC}} = 55 \text{ kpc}$, $3.1 \times 10^5 \text{ stars/degrees}^2$ at $R_{\text{GC}} = 35 \text{ kpc}$ and $2.9 \times 10^6 \text{ stars/degrees}^2$ at $R_{\text{GC}} = 15 \text{ kpc}$ for the halo of M31. These densities are ≈ 10 times higher than the densities obtained by Pearson et al. (2019) at the same radial distances and a similar *Roman* magnitude cut. We note that our methods for estimating the foregrounds

significantly deviate from the original methodology by [Pearson et al. \(2019\)](#), by incorporating a stellar density model and by scaling the stellar density to the brighter regions of the CMD where the PAndAS survey is most complete. In contrast, within the magnitude limits of the PAndAS data ($g_0, i_0 \approx 26$), our simulated densities of 2.0×10^4 stars/degrees², 2.2×10^4 stars/degrees² and 9×10^4 stars/degrees² at $R_{GC}=55$ kpc, 35 kpc, and 15 kpc, respectively, are in agreement with the observed densities in PAndAS at the same galactocentric radii. The agreement between our simulation and the observed data validates our assumptions about the background and foreground populations. We further discuss the limitations of our simulations in Section 5.

3.1.3. Simulating Observed Stars in Pal 5

We simulated the stream population in a similar manner to the backgrounds, but in this case, scaling to the observed properties of Pal 5. We generated a sample of 10^6 stars assuming a power-law IMF ($dN/dM \propto M^{-0.5}$, [Grillmair & Smith 2001](#); [Ibata et al. 2017](#)). We then assigned CFHT g and *Roman* R , Z absolute magnitudes by interpolating the PARSEC isochrones for an age of 11.5 Gyr and $[Fe/H] = -1.3$. We applied a distance modulus corresponding to Pal 5 ($d_{mod} = 16.85$; [Pearson et al. 2019](#)), and then determined a population normalization factor by comparing the distribution of simulated CFHT g magnitudes to the 3000 stars with $20 \leq g \leq 23$ that are known members of the Pal 5 stream ([Bonaca et al. 2019](#)). With this normalization factor, we computed the number of stream stars detectable in a given host galaxy based on the corresponding distance modulus and *Roman* magnitude limit. Our number count predictions for Pal 5 match the predictions of [Pearson et al. \(2019\)](#).

To generate a final simulated *Roman* image, we resampled the simulated streams described in Section 2.3, drawing only the expected number of detectable stars for our *Roman* Z -band limits as a function of distance. We also drew foreground and background stellar fields at the same Z -band limits, the latter sampling the three galactocentric radii from M31 PAndAS data, as well as different host galaxy distances. For simplicity, the positions of background and foreground stars were assumed to be uniformly distributed for a given 10 kpc by 10 kpc patch. As most background halo stars are of similar stellar populations as the stellar stream stars, the detection of these streams and their gaps depends mostly on density contrasts. We, therefore, focus our analysis on star count maps of these fields, rather than simulated images that incorporate brightness and instrumental point spread function effects. Figure 3 shows examples of our simulations of streams in M31. Henceforth, we will use

“mock observations” or “density maps” to describe the results of our simulations.

3.2. Gap Identification by Visual Inspection of Density Maps

We now turn to examining gaps and quantifying their detection with distance and exposure times. [Pearson et al. \(2019, 2022\)](#) developed methods for finding Pal 5-like streams in *Roman* observations. Our primary goal is to investigate the detection of gaps, assuming the stream has already been identified. We present the visual inspection of gaps from simulated streams in M31 (Figure 3) and other external galaxies (Figure 4), centering the density maps on the gap region. For simplicity, we only considered gaps from interactions with subhalos of $5 \times 10^6 M_{\odot}$ as this mass is in the appropriate range for testing different dark matter models ([Bullock & Boylan-Kolchin 2017](#)); and gaps that resulted from these interactions are clearly visible in mock streams (Figure 1). In all of our simulated observations, we applied a photometric metallicity constraint of $[Fe/H] < -1$, as GC streams are typically metal-poor (e.g. [Martin et al. 2022](#)), allowing us to reduce the number of background stars. In real *Roman* images, selecting low-metallicity stars will require fitting the foreground populations of a given galaxy to synthetic isochrones.

The angular lengths of Pal 5 streams for galaxies within a ≈ 1.2 Mpc volume are larger than the field of view of the *Roman* telescope; hence, only a portion of the stream will fit inside a *Roman* field for these distances. For an M31 distance of 770 kpc ($d_{mod} = 24.4$, [Ibata et al. 2014](#)), the projected angular distance is 13.4 kpc/degree, making the angular size of Pal 5-like streams in M31 (lengths of 7.8–12 kpc, [Pearson et al. 2019](#)) equal or larger than the expected 0.52 degree \times 0.52 -degree *Roman* field of view. Visually, the density contrast between the stream and background stars increases with galactocentric radius and with exposure time. [Pearson et al. \(2019\)](#) estimated that the width of a Pal 5-like stream in M31 would vary between 0.053 kpc–0.127 kpc at a galactocentric radius (R_{GC}) of 15 kpc–55 kpc, and the length would vary between 7.8 kpc and 12 kpc. We could best identify the gaps in the density maps for 1-hour exposure, otherwise, visual identification of the stream and gaps is difficult (see Figure 3).

To simulate streams in other external galaxies with distances spanning 0.5 Mpc to 10 Mpc (assuming a similar stellar composition and tidal field as M31), we offset the M31 background population in the *Roman* CMD space to the appropriate distance modulus, retaining

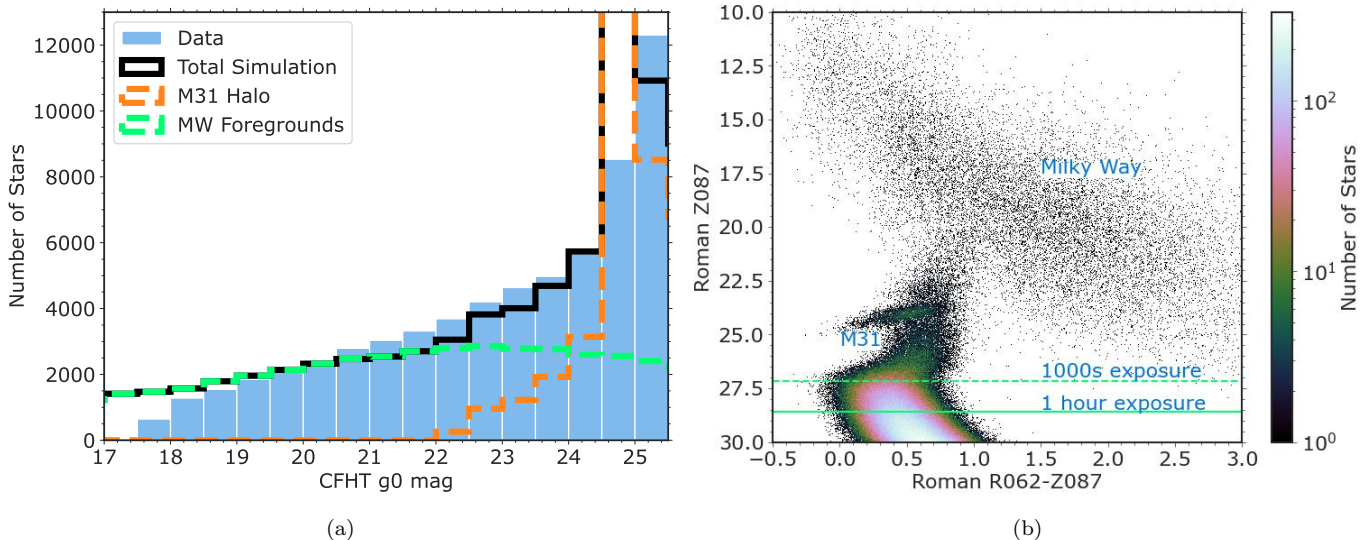


Figure 2. Colors and magnitude distributions of our simulations compared to the data. (a): CFHT g_0 mag luminosity function based on the PAndAS data (blue filled-in histograms) and our simulations (black) for populations at $R_{GC}=35$ kpc. The simulations are further divided into Milky Way foregrounds (light green) and M31 stars (orange). We are able to reproduce the CFHT g -band luminosity function based on our scaling to the CFHT CMD (more details in Appendix A) (b): Simulated color-magnitude diagram for *Roman* R and Z bands at $R_{GC}=35$ kpc. CMD regions that are dominated by M31 stars or Milky Way foregrounds are labeled in blue text. The horizontal dashed and solid lines show the magnitude cuts for 1000 s and 1 hr exposures, respectively. With these magnitude cutoffs, the M31 halo population will be primarily dominated by horizontal-branch stars and giants.

the same Milky Way foreground populations. The number of stars in Pal 5 was re-sampled to match the pre-computed number of stars at the new galactic distance. We applied the same magnitude cuts as our simulated foreground and background models.

Figure 4 compares the simulated streams, all placed at a fixed galactocentric distance of 35 kpc. We display a fixed area in physical units of $7 \text{ kpc} \times 4 \text{ kpc}$ in the figure (7 kpc is \approx half the length of the stream), which corresponds to smaller angular scales in the total *Roman* field of view at larger distances. We display the streams at $R_{GC}=35$ kpc because the combination of the density contrast and the thickness of the stream makes it easier to visually detect the gap in these mock observations compared to images at 15 kpc and 55 kpc. As the distance to the host galaxy is increased, the density of both background stars and the stream decrease. We note that the background stellar densities fall off faster than the density inside the stream with galaxy distance, due to the choice of isochrones and the metallicity cuts that we are applied to the data. We caution that in real observations, other external galaxies will have different sizes, and their halos will have a different composition compared to M31. All these caveats are further discussed in Section 5.

Through a visual inspection of streams with gaps in host galaxies spanning a distance of 0.5 to 10 Mpc, we

find that the gap is visible by eye in external galaxies at distances out to ≈ 1.5 Mpc (see Figure 4).

4. AUTOMATING THE DETECTION OF A GAP

Visual confirmation alone can result in biased assessments of stream and gap detection, hence we now turn to quantifying detection using an automated tool. In Sections 4.1 and 4.2 we lay out methods for defining the gap and the stream region, and in Sections 4.3, 4.4, and 4.5 we outline a procedure for quantifying the detection of each gap and we provide a detection limit as a function of distance using a large sample of simulated mock streams.

4.1. Density Estimation and Detecting Gaps

Previous studies have developed algorithms to find and characterize stellar streams in the Milky Way (e.g., Mateu et al. 2017; Malhan & Ibata 2018; Shih et al. 2022, 2023) and in external galaxies (e.g., Hendel et al. 2019; Pearson et al. 2022). Once such algorithms have determined a stream’s presence, location, extent, and orientation, we can then search for gaps. We used the gap-finding tool (Contardo et al. 2022, FindTheGap), which is designed to evaluate under-densities in multi-dimensional data. Gaps, just like streams, can be detected by eye, but this tool provides an automated approach and serves as an additional method for confirmation or rejection in conjunction with visual detection.

Table 3. Summary of Simulations Parameters for Resolved Stellar Populations

Population	Quantity	Distribution	Reference
Foregrounds & backgrounds	IMF	Kroupa ^a	Kroupa (2001)
Milky Way Thin Disk	age	Uniform (0, 8) Gyr	Jurić et al. (2008)
	[Fe/H]	Uniform (-1,0.5)	Mackereth et al. (2019)
	spatial density	Exponential ^b (H= 350 pc, L= 2600 pc)	Jurić et al. (2008)
Milky Way Thick Disk	age	Uniform (8, 10) Gyr	Kilic et al. (2017)
	[Fe/H]	Uniform (-1,0.5)	Hawkins et al. (2015)
	spatial density	Exponential (H= 900 pc, L= 3600 pc)	Jurić et al. (2008)
Milky Way Halo	age	Uniform (10, 13) Gyr	Jofré & Weiss (2011)
	[Fe/H]	Uniform (-2.5, -1)	Mackereth et al. (2019)
	spatial density	Spheroid ^c (n= 0.64, q= 2.77)	Jurić et al. (2008)
M31 Halo	age	Uniform (5, 13) Gyr	Ibata et al. (2014)
	[Fe/H]	Uniform (-2.5, 0.5)	Ibata et al. (2014)
	spatial density	Spheroid ^d (n= 1.11, q= 3)	Ibata et al. (2014)
Pal 5	age	11.5 Gyr	Ibata et al. (2017)
	[Fe/H]	-1.3	Ibata et al. (2017)
	IMF	dN/dM= $M^{-0.5}$	Grillmair & Smith (2001)

^a $dN/dM = M^{-\alpha}$, with $\alpha = 1.3$ for masses between $0.08 M_{\odot}$ and $0.5 M_{\odot}$, $\alpha = 2.3$ for masses > 0.5 .

^b Exponential profile defined in Equation 9.

^c Spheroidal profile defined in Equation 10.

^d Profile given by Equation 11.

FindTheGap uses the projection of the second derivatives (Hessian, \mathbf{H}) of the density estimate onto the orthogonal subspace of the density gradient vector (g), denoted as $\mathbf{\Pi H \Pi}$, where $\mathbf{\Pi}$ is a projection matrix defined as:

$$\mathbf{\Pi} = 1 - \frac{gg^T}{g^T g} \quad (12)$$

The maximum eigenvalue of $\mathbf{\Pi H \Pi}$ can then be used as a statistic to estimate if a point in the data space is “in a gap”. Conversely, the minimum eigenvalue of $\mathbf{\Pi H \Pi}$ can be used to highlight ridges and overdensities. The density estimation depends on a free parameter, the bandwidth, which relates the estimated density to the spacing between data points. In addition to the bandwidth, the stability of the gap detection also depends on the number of data points.

To apply this tool to simulated observations, we started with simulated density maps (Figures 3 and 4), making a cutout centered on the visually-identified gap. We did not use the full *Roman* field of view as the angular size of the stream becomes progressively smaller at larger galaxy distances, making it more difficult to identify gaps. We then created a grid of 50 by 20 points along each cutout with uniform spacing, covering an area of

5 kpc \times 2 kpc that includes the main track of the stream and surrounding foreground and background stars.

The accuracy of this method relies on the choice of bandwidth. Large bandwidths tended to smooth over structures in the data, including the gap, but small bandwidths introduced gaps and other small-scale structures that were not necessarily present in the underlying true density. Additionally, the density estimation in **FindTheGap** assigns lower densities to regions near the edge of the simulated mock observations. To avoid these edge effects, we first ran an estimation of the stellar density and the values of $\mathbf{\Pi H \Pi}$ on a slightly larger dataset, incorporating stars beyond the specified grid. Specifically, we required the data bounds to be larger than grid bounds to a factor of twice the bandwidth. For example, we used a 9 kpc by 6 kpc region for a bandwidth of 1 kpc, given our fixed grid size of 5 kpc by 2 kpc. After we fit the density estimator to the data, we predicted the values of density and $\mathbf{\Pi H \Pi}$ on the smaller 5 kpc by 2 kpc grid (see Figure 5). To ensure the fidelity of each gap detection and to remove spurious gaps, we ran this estimation five times for every simulation, choosing the same number of randomly selected stars for each estimation (bootstrap re-sampling). In each iteration, the

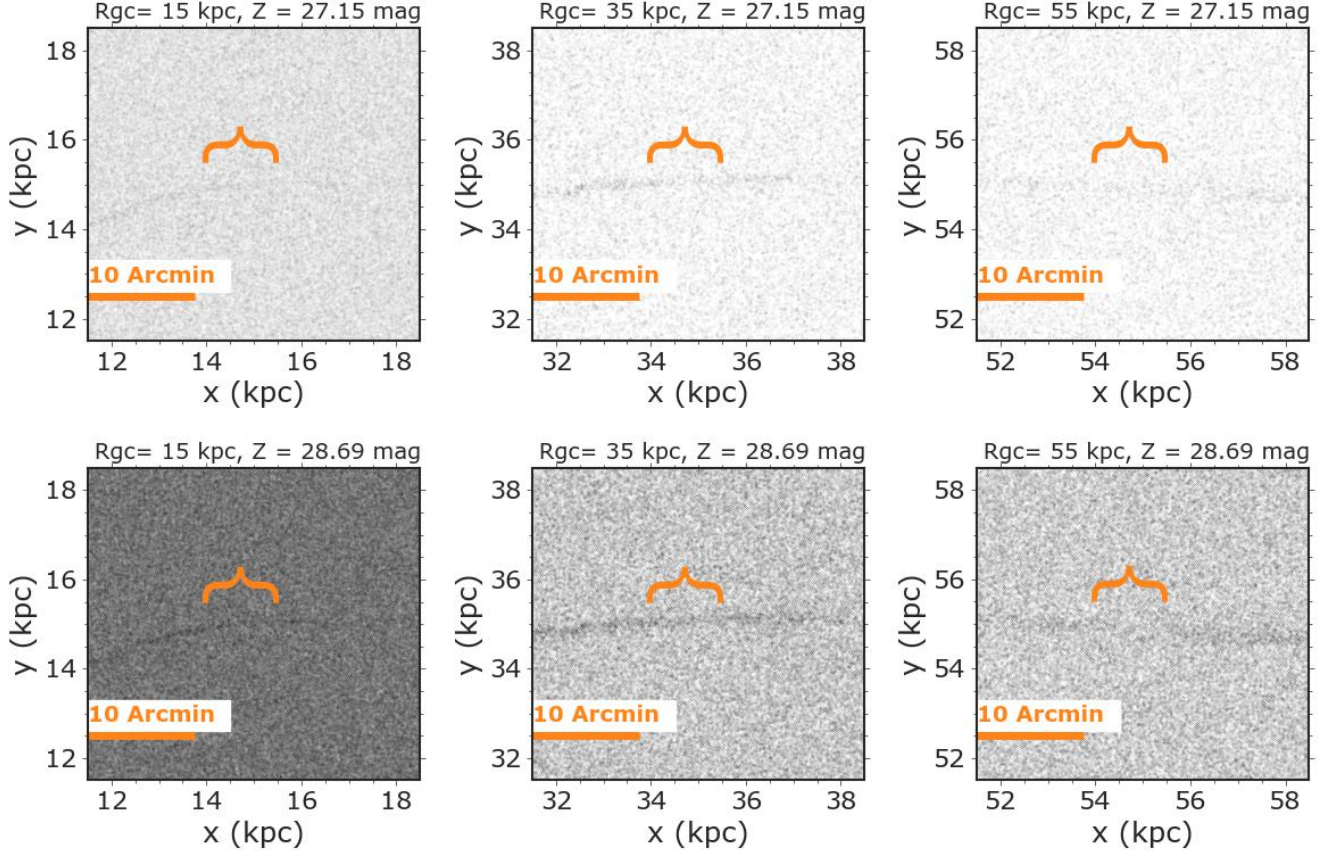


Figure 3. Simulated stellar density maps for a full *Roman* field of view of 0.28 deg^2 with M31 background stars and Milky Way foregrounds. The gap in the stellar stream is caused by an interaction with a subhalo with a mass of $5 \times 10^6 M_{\odot}$, and only a portion of the stream is shown here. The streams are injected at galactocentric distances of 15 kpc, 35 kpc and 55 kpc, and exposure times are 1000s ($Z = 27.15$, top panels) and 1 hr ($Z = 28.69$, bottom panels). We display these maps in physical coordinates to highlight the scale of the gap, indicated by curly brackets. The projected x and y coordinates in kpc were computed by assuming the distance to M31 is 770 kpc (an angular scale of 13.4 kpc/degree). We can visually see the gap for 1-hour exposure, otherwise, it becomes more obscured by the background population.

density, and the minimum and maximum eigenvalues of $\Pi H \Pi$ were scaled to span values of 0 and 1 to maintain a consistent range across bootstrap samples. We then computed the final $\Pi H \Pi$ map by taking the median over all bootstraps. Figure 5 shows the result of the application of this tool for simulated observations at a distance of 1 Mpc. The map of $\Pi H \Pi$ eigenvalues reliably locates the gap and the stream. We further discuss our determination of the optimal bandwidth in Section 4.4.

4.2. Further Outlining the Stream and Gap Regions with Indicator Points

In principle, it is possible to determine the stream path from the minimum eigenvalues of the $\Pi H \Pi$ matrix as the stream represents an overdensity. Nevertheless, our focus was solely on the detection of gaps within a stream. We constrained the stream region inside the

density maps by fitting a second-degree polynomial to the pre-determined positions of the injected stream. To define the stream track, we fixed the size of the stream to be 0.2 kpc, which exceeds the real width of the stream (visually and based on analytical calculations by Pearson et al. 2019). This is to ensure that there were enough grid points to cover the full stream region. This step also allows us to measure the density of stars inside the stream, later discussed in Section 4.5. We note again that our assumption is that the stream has been observed, and the approximate stream region is therefore known.

To outline the gap region, we selected points on the grid falling within the top 95-percentile of the distribution of minimum eigenvalues of $\Pi H \Pi$. We will refer to the regions on the grid that match this criterion as “gap indicator points”. As shown in Figure 5, this criterion provided a first-order estimation of the location of

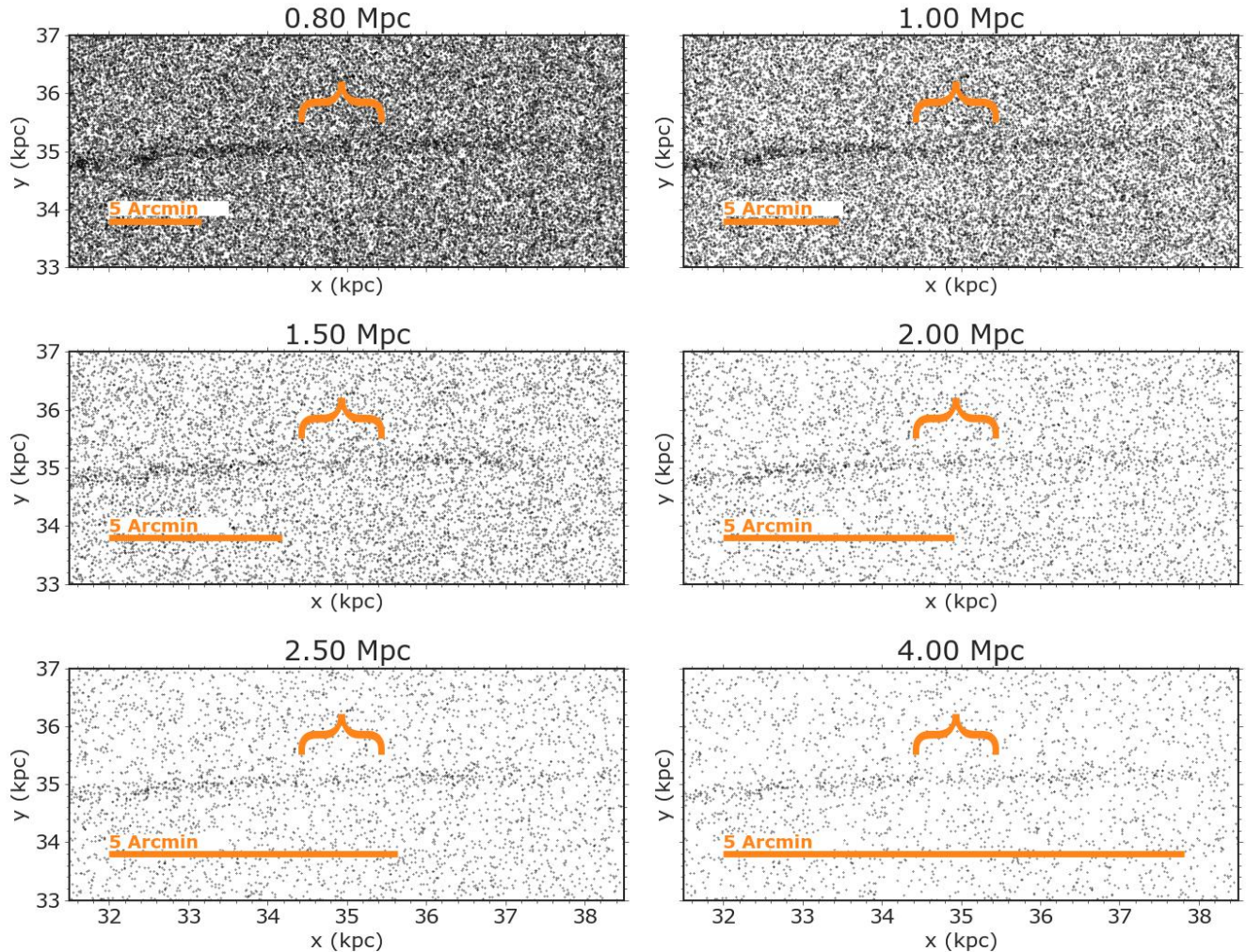


Figure 4. Mock observations of streams with gaps in a segment of the full *Roman* field of view. To generate these mock observations, streams were injected into pre-computed backgrounds. Stars are plotted with the same symbol size to facilitate comparison at various galaxy distances. The sizes of the images are $7 \text{ kpc} \times 4 \text{ kpc}$ (about half the length of the stream), which would correspond to different angular sizes on the sky depending on the distance of the observed galaxy. The horizontal bar shows the scale of 5 arcmin (or $1/6$ of the $32 \text{ arcmin} \times 32 \text{ arcmin}$ full *Roman* field of view). We show the halo of the galaxy at $R_{\text{GC}} = 35 \text{ kpc}$, assuming an exposure time of 1 hour ($Z = 28.69$) and a perturbation in the stream from $5 \times 10^6 M_{\odot}$ subhalo. We can see gaps to a distance of $\approx 1.5 \text{ Mpc}$.

the gap. We then further constrained the gap region to be centered around the median position of gap indicator points, with a width equal to the size of the stream region and a length equal to the gap size (see Section 2.4). This definition of the gap region along with gap indicator points was later used to develop metrics for distinguishing successful detections from noise.

Figure 5 illustrates the gap detection procedure. As all the mock observations were converted to physical projected coordinates, this assumption yielded consistent gap identification with galaxy distance. We further discuss our quantification of the breakdown of the gap identification procedure in the upcoming sections.

4.3. Defining Metrics for Gap Detections

We now turn to discuss our application of the gap detection method on a sample of mock streams in an automated fashion. We created an automatic pipeline using the methods described in Section 4.1 to search for gaps in simulated mock streams, and two metrics to quantify the detections. First, we computed $\Pi H \Pi$ maps and their eigenvalues for mock observations spanning distances between 0.5 Mpc and 10 Mpc and using bandwidths between 0.1 kpc and 2 kpc for all three R_{GC} values. We restricted the bandwidth range to 2 kpc as the metrics discussed below did not improve beyond this range. Ultimately bandwidths between 0.5 kpc and

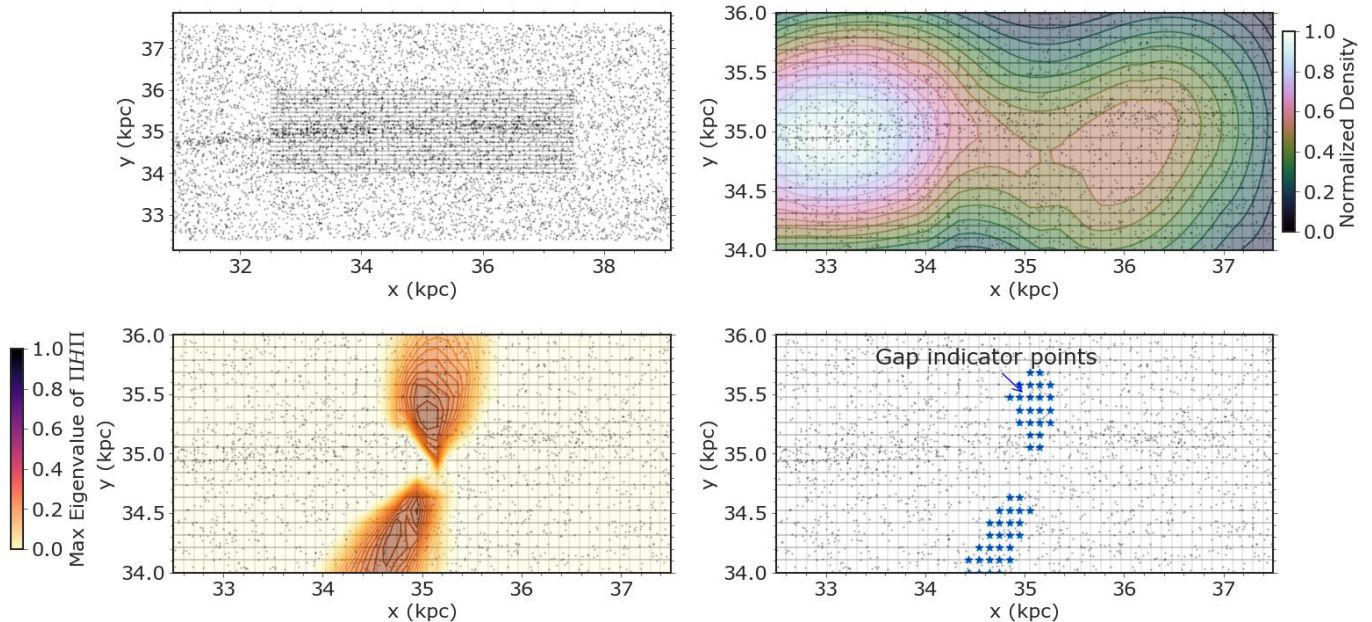


Figure 5. Illustration of the gap detection tool with a fixed bandwidth of 0.8 kpc applied to a stream at $R_{GC} = 35$ kpc and a distance of ≈ 1 Mpc for a 1000 s exposure. Note that we assume all stars are resolved. *Top Left:* Black dots show the stream and uniformly-distributed background stars in the vicinity of the stream. We used a fixed grid of 5 kpc by 2 kpc indicated by black lines. *Top Right:* Contours show the stellar density which clearly shows an underdensity near the gap region and a decrease in density towards the edge of the stream. The density estimation is applied over the full range of the data to avoid edge effects at the end of the grid (see text for discussion). *Bottom Left:* Contours show a map of the maximum eigenvalues of $\Pi H \Pi$, which are maximized near the gap. We used this map to indicate the location of the gap along the stream. *Bottom Right:* Gap indicator points are shown in blue as defined to be where the maximum eigenvalues of $\Pi H \Pi$ are in the top 95 percentile. This procedure can locate underdensities inside the stream.

1 kpc were optimal in finding the gap region. For each step, we repeated the generation of the stream, the generation of background populations, and the gap detection process to account for the scatter in the detection metrics at low stellar densities. This process resulted in 81,795 independent mock observations.

We used three metrics to quantify the significance of each detection. To quantify the uncertainty in the gap detection, we defined the spread of all the gap indicator points (\mathcal{S}_g) as the range of their x-positions (max-min). As a reminder, “gap indicator points” were defined as points on the grid in the top 95 % of maximum eigenvalues of $\Pi H \Pi$. We anticipate that a robust gap detection has low \mathcal{S}_g values, as these gap points would be concentrated around one point near the stream (see blue markers in the lower right panel of Figure 5).

We then computed the median value of the absolute difference between the x-positions of gap indicator points to the center of the density maps denoted by Δ , computed for each stream separately. As we designed each simulated observation to be centered around the gap, we expect optimal detection to have a small value for Δ . Nevertheless, we show in Appendix B.3, that our pipeline can also identify gaps located away from

the center. After we defined \mathcal{S}_g and Δ per stream, we used these metrics to determine which bandwidths were optimal for detecting gaps.

4.4. Determining the Optimal Bandwidth

The effects of bandwidth choice on the gap detection metrics as a function of distance are shown in Figure 6. We found that bandwidths between 0.5 kpc and 1 kpc resulted in the lowest values for the spread of gap indicator points (\mathcal{S}_g) and the deviation of the location of the gap from the center of the density maps (Δ). For large bandwidths, the estimated density on the grid is centrally concentrated and features are washed out. For small bandwidths, the stellar density was fragmented into small groups of spurious gaps, which also resulted in large values for \mathcal{S}_g and Δ . We illustrate these effects in Appendix B.2. We inferred a middle value of ≈ 0.8 kpc as our optimal bandwidth.

To further evaluate the performance of the gap-detection tool and to ensure that our pipeline was robust, we also applied the gap-finding tool to mock observations with an intact stream (without a gap from an interaction with a subhalo) using our described methodology. As shown in Appendix B.3, we could identify the drop off in density towards the edge of the stream,

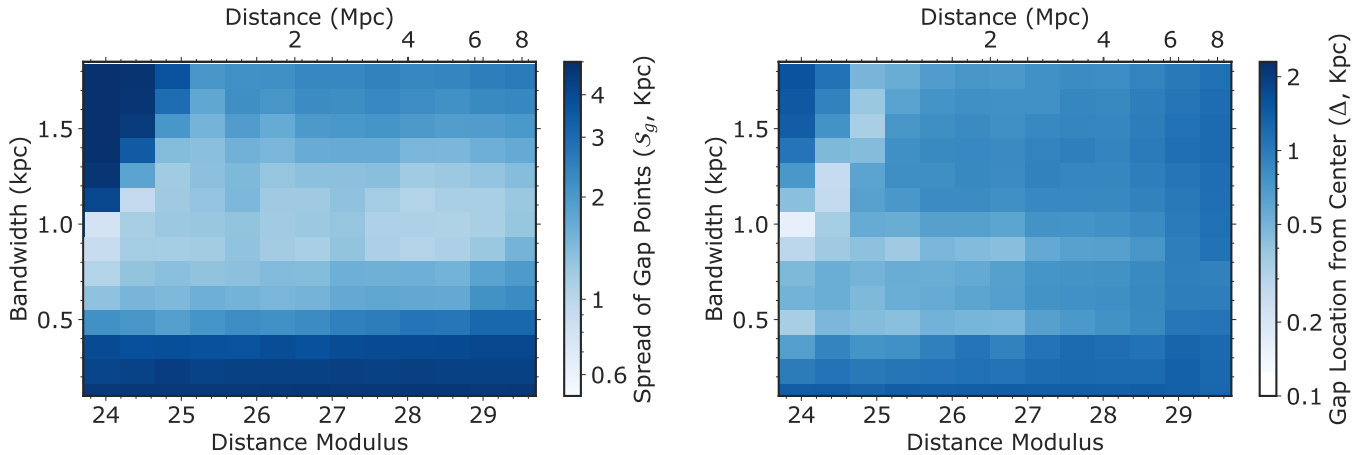


Figure 6. Distribution of detection metrics for a gap from a subhalo of mass equal to $5 \times 10^6 M_{\odot}$. *Left:* Distribution of the spread of gap indicator points (\mathcal{S}_g) defined as the range (max-min) of their x-values. There is an island of best bandwidths between 0.5 kpc and 1 kpc where this metric is the lowest, which defines our optimal set of bandwidths. *Right:* Map of the median deviation of gap indicator points with respect to their true location (Δ). The combination of Δ and \mathcal{S}_g values show that the optimal bandwidth for locating the gap is between 0.5 kpc and 1 kpc.

but we could not identify any gaps inside the track of the unperturbed stream for a bandwidths ranges of 0.5 to 0.9 kpc, further validating our method. In practice, when applying this tool to real *Roman* images, the optimal bandwidth may depend on the scale of underdensities in the backgrounds and a positive detection would require further characterization. Our goal in this study is to provide an additional methodology for detecting gaps in conjunction with visual inspections. While our pipeline could lead to false positives, it is unlikely to miss any real gaps in the data.

4.5. Distance Limits for Gap Detections

To determine a tentative detection limit, we used both the density of stars inside the gap region and the location of the gap region as a reference. We estimated the stellar density inside the stream and the gap by counting the number of stars inside each region and dividing this number by the physical area (in kpc^2) (see Section 4.4 for the definition of the gap and stream points/regions). To determine the area of the stream region, we multiplied the total area of the grid (10 kpc^2) by the fraction of grid points that fell within each respective region. Because the stream track did not follow a simple straight line, this procedure allowed us to obtain a more accurate measurement of each region’s area. For the gap region and the background region, we approximated the area as a rectangle. For the gap, we used a width equal to the width of the stream, and the pre-computed length; and for the backgrounds, we used a width of 0.5 kpc and a length of 5 kpc.

Figure 7 shows the surface densities (number/ kpc^2) inside the stream region, the gap, and the background

for a fixed optimal bandwidth of 0.8 kpc. There is a monotonic decrease in the surface density inside the stream, inside the gap, and in the background with increasing galaxy distance, as expected. The stream density is generally higher than the gap density and the background. Additionally, streams at smaller R_{GC} values are denser than streams at larger R_{GC} values. However, it was still difficult to determine the detection limits from these densities alone.

To establish a tentative detection limit for our pipeline, we examined the evolution of the gap location with distance. We plot the median value of the location of gap points (Δ) for 5 random streams for each distance step in the bottom panels in Figure 7. Our expectation is that for robust detections of gaps, the central gap location will remain stable across several iterations. While there was a systematic offset between the center of the stream from the true center, we observed this “flaring” for the value of Δ at larger distances. For both 1000 s and 1 hour exposure times, this effect translates to distance limits of 2 Mpc–3 Mpc. In Appendix B.1, we show examples of gap detections in mock streams at $R_{GC}=35$ kpc which also indicates that the location of the gap inside the stream becomes progressively uncertain beyond these distance limits.

To summarize, we used the tool (*FindTheGap*) developed by Contardo et al. (2022) to evaluate the detection of gaps beyond a simple visual inspection and to quantify the distance limit with exposure time. We applied this tool to a set of $> 80,000$ mock observations for galaxy distances between 0.5–10 Mpc with M31-like stellar populations as background stars. For each mock observation, we defined “gap indicator points” based on

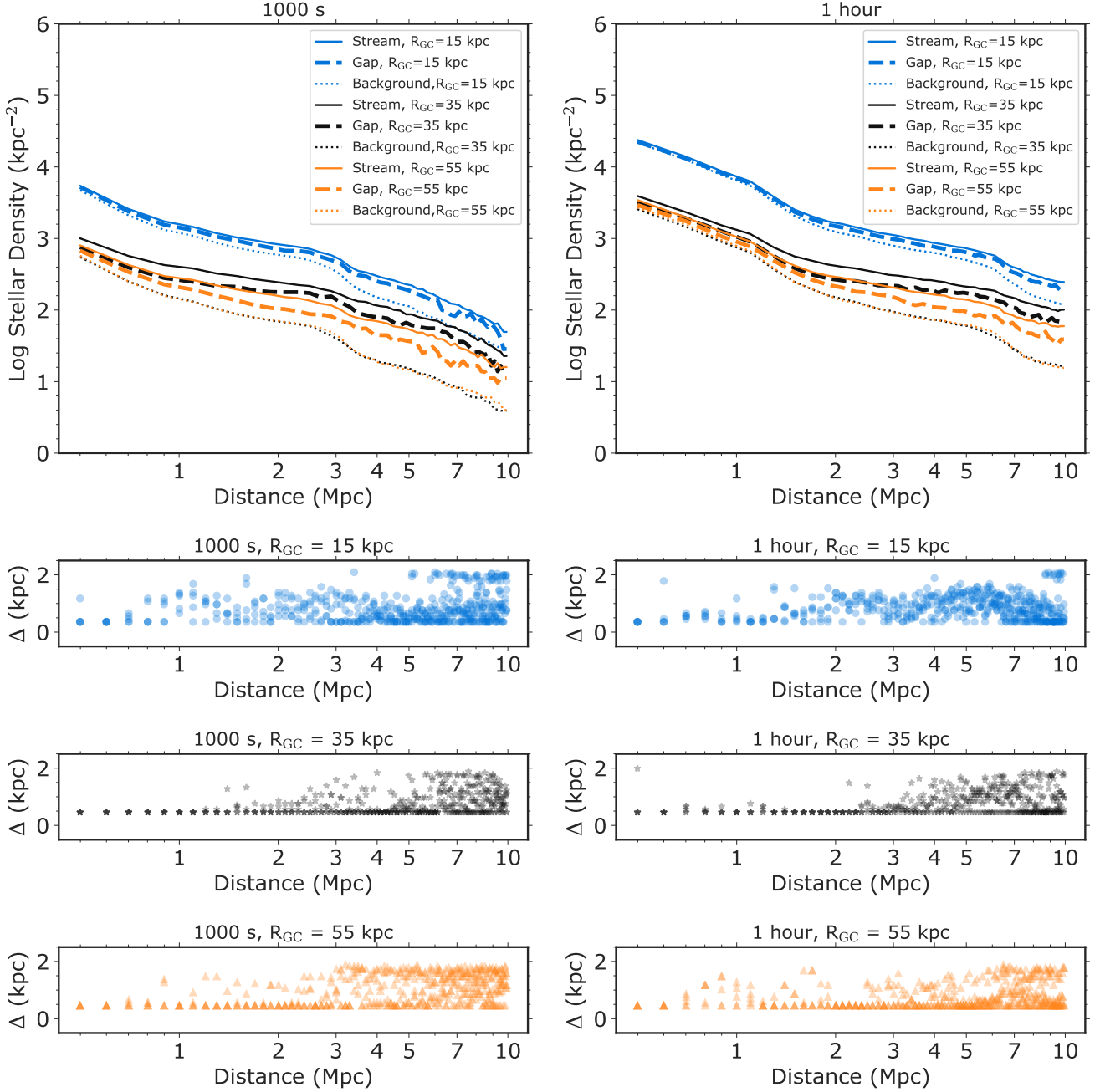


Figure 7. Testing the stability of gap detections with distance using the optimal bandwidth of 0.8 kpc. *First row:* Variation in the distribution of stellar densities inside the stream and the gap with distance. Gaps were created from subhalos of masses of $5 \times 10^6 M_{\odot}$. The density of stars in kpc^{-2} for the stream region is shown with solid lines, the gap is shown with dashed lines, and the background is shown with dotted lines a 1000 s (left) and 1-hour exposure (right) for galactocentric radii of 15 kpc (blue), 35 kpc (black) and 55 kpc (orange). As a general trend, the density inside the stream is higher than the gap, and the background density but it is difficult to establish a detection limit from densities alone. *Last 3 rows :* Value of the absolute difference between the x-positions of gap indicator points and the center of the density maps (Δ) as a function of distance for a 1000 s exposure (left) and 1-hour exposure (right). The color scheme follows the same pattern as the top panels. We defined our gap-detection limits to be where the median value of Δ starts to fluctuate, which corresponds to 2–3 Mpc.

gap statistic provided by `FindTheGap`. The gap detection method relies on the bandwidth as an additional parameter to compute the density of stars on a pre-defined grid. By changing this parameter uniformly between 0.1–2 kpc, we determined that the optimal bandwidth for detecting gaps was ≈ 0.8 kpc. We then evaluated the effectiveness of each detection by estimating the central location of gap indicator points with galaxy distance. Results from this procedure pipeline suggest that gaps from subhalos of $5 \times 10^6 M_\odot$ in the halo of M31-like galaxies will be detectable to 2–3 Mpc for exposure times between 1000s and 1 hour.

5. DISCUSSION

In this Section, we revisit assumptions in our numerical simulations (Section 5.1), the observational limitations (Section 5.2), their implications, and how they affect our results. We also discuss future prospects of using extragalactic streams for dark matter science (Section 5.3).

5.1. *Limitations in Our Simulation of a Gap*

In our simulations, we have assumed that the galactic potential is smooth and static. However, previous studies of the Milky Way have shown that inhomogeneities in the global potential, including giant molecular clouds, galactic bars, streams, other globular clusters, and spiral arms can perturb GC streams (Amorisco et al. 2016; Hattori et al. 2016; Price-Whelan et al. 2016; Erkal et al. 2017; Pearson et al. 2017; Banik & Bovy 2019; Doke & Hattori 2022). To mitigate this effect, we can search for streams located at large galactocentric radii in external galaxies, and where the contrast between the stellar stream and background is more dramatic (see Figure 3). In addition, at large galactocentric radii, bars, spirals, and molecular clouds are less likely to cause dynamical perturbations in streams. Furthermore, with larger sample sizes we will be able to determine the frequencies, sizes, and locations of underdensities in streams, which gives us the ability to statistically evaluate signatures of perturbations from dark matter subhalos.

Global potentials in galaxies are also deformed by mergers and satellite interactions (Weinberg 1998; Garavito-Camargo et al. 2019), and observations suggest that M31, in particular, has been largely shaped by a possibly recent minor (or major) merger (D’Souza & Bell 2018; Escala et al. 2021; Dey et al. 2022; Bhattacharya et al. 2023). Merger events and interactions with satellites can distort present streams (Erkal et al. 2019; Shipp et al. 2021; Lilleengen et al. 2023) and contribute to the accretion of new globular clusters that will eventually form streams (Kruijssen et al. 2020). The details of the formation and disruption of GC streams have

not been extensively explored in large cosmological simulations.

Throughout this work, we have only considered one encounter between the stream and the subhalo. Old GC streams can undergo multiple collisions with subhalos, creating multiple observable density fluctuations and perturbations to the stream morphologies. In fact, multiple under-densities have been observed in several Milky Way streams such as GD-1, (Bonaca & Hogg 2018) and Pal 5 (Erkal et al. 2017). We do not further explore the effects of multiple encounters here, but based on our analysis of the detectability of a gap from a single subhalo encounter, we expect that streams, which have undergone multiple interactions with subhalos to have multiple observable gaps that can be detected using our methodology. Using realistic galaxy simulations that include baryonic physics, Barry et al. (2023) predicts that Pal-5-like streams in the Milky Way could undergo 2–3 interactions/Gyr with subhalos of masses $> 10^6 M_\odot$ before dissolution.

In our analysis, we limited our investigation of the observability of gaps with *Roman* to subhalo encounters between GC streams and dark matter subhalos with Hernquist profiles (Hernquist 1990). Cuspier profiles for the dark matter subhalo can result in larger gaps for the same encounter properties (Sanders et al. 2016). Additionally, as gaps grow with time, the initial size and the growth of gaps will depend on the collision parameters, such as the mass and scale radius of the subhalo, the relative velocities of the subhalos to the stream, the impact parameter, the stream orbit, the time of the collision, the impact position, and others. These parameters have been extensively explored in numerical and analytical work (Yoon et al. 2011; Erkal & Belokurov 2015; Sanders et al. 2016; Koppelman & Helmi 2021). In external galaxies, these effects will be difficult to disentangle given the lack of kinematic information. However, large statistical sample sizes of observed gaps will allow for rigorous comparisons to predictions of gaps in streams evolved within various dark matter frameworks (e.g., warm, fuzzy, self-interacting).

5.2. *Limitations in Our Simulation of Mock Observations*

In this work, we have generated mock *Roman* observations to mimic stellar halos of external galaxies at various distances without accounting for observational biases due to crowding, extinction, or star/galaxy separation. Pearson et al. (2019) discussed several of the limitations and considerations to take into account for such mock observations. In particular, they concluded that crowding effects will not affect the detection of thin

GC streams in external galaxies with *Roman*. We can further minimize crowding effects by observing external galaxies with sight-lines pointing away from the Milky Way’s galactic plane. Our method relies on estimating the underlying density of stars, thus measuring the density contrast between stream stars and background stars is the determining factor in the success of gap detections. Additionally, the effect of dust extinction will be minimal for the halo of M31 at infrared wavelengths (Dalcanton et al. 2015).

In addition, Pearson et al. (2019) evaluated the feasibility of star/galaxy separation detection on the detection limits of GC streams with *Roman*. They used the Space Telescope Image Product Simulator (STIPS) to inject known galaxy catalogs into simulated fields and applied quality cuts based on source shape. They concluded that including background galaxies would limit the detection of Pal 5 in M31-like galaxies to 1.1 Mpc–1.8 Mpc for an exposure time of 1 hour. There are ≈ 115 galaxies in this volume based on Karachentsev & Kaisina (2019), and gaps will be detectable to these distances based on the methodology presented in this work. Assuming “perfect” star/galaxy separation and investigating GC streams with 5 – 10 times more massive than Pal 5, they estimated that thin GC streams could be detected in host galaxies out to 6.2 – 7.8 Mpc with a 1-hour *Roman* exposure. This volume contains ≈ 660 galaxies (Karachentsev & Kaisina 2019), with 25 galaxies that are 10% more luminous than the Milky Way; and the vast majority of galaxies within the 7.8 Mpc limit are dwarf galaxies. While we did not include such an analysis in this paper, we expect the feasibility of star/galaxy separation to have a similar effect as the predictions by Pearson et al. (2019) on the detection of gaps as the detection of streams because background galaxies will be randomly spread out throughout the image. We note that the formation of GC streams in dwarf galaxies has been explored in simulations (e.g. Peñarrubia et al. 2009), but more work is needed to estimate their observability.

Finally, future large observing programs dedicated to searching for gaps in streams in external galaxies can extend to longer exposure times, which would allow for larger sample sizes and potential detection of GC streams in dwarf galaxies. Optimistically, it is likely that a full program that is dedicated to observing these gaps with *Roman* would extend over several hours of observing time, allowing the stacking of images from multiple visits to reach depths beyond our estimates.

5.3. Inference of Dark Matter Properties and Expected Sample Sizes

Our focus throughout this paper has been on the detectability of underdensities in extragalactic GC streams. Previous studies have explored pathways to isolate dark matter effects from baryonic effects and to infer dark matter properties (e.g. particle mass) from observations of gaps in streams. Using linear perturbation techniques, Bovy et al. (2017) constrained the number of dark matter subhalos of masses between $10^{6.5}$ and $10^9 M_\odot$ within 20 kpc of the Milky Way’s galactic center by modeling Pal 5 data (see also Banik et al. 2021). Banik & Bovy (2019) provided a powerful method for disentangling underdensities caused by dark matter subhalos from baryonic perturbers (e.g. bars, molecular clouds, and spiral arms) in Pal 5 by computing the various perturbers’ contributions to the stream’s density power spectrum. They concluded that the contribution from spiral structure to Pal 5 substructure is low but that giant molecular clouds can create small-scale underdensities comparable to those from dark matter subhalos (Amorisco et al. 2016). Recently, Hermans et al. (2021) showed that simulation-based inference techniques with machine learning that map observed densities in streams to simulations can help constrain dark matter structure. They found that GD-1 stream data can be used to constrain warm dark matter particle masses and distinguish between CDM and WDM models. Lovell et al. (2021) confirmed that the structure in GD-1 and Pal 5 can place limits on the fraction of WDM vs CDM subhalos within a 40 kpc distance from the Galactic center (see also discussion by Pearson et al. 2019, 2022). Searching for streams in the halos of external galaxies far from the bar and star-forming regions will increase the likelihood of finding gaps induced by gravitational perturbations from dark matter substructure, which can be compared to expectations from various dark matter candidates.

Even though we have shown that *Roman* will not be able to detect gaps in GC streams in external galaxies further than 2–3 Mpc away, in M31 alone there are ≈ 450 GCs (Galleti et al. 2006, 2007; Huxor et al. 2008, 2014; Caldwell & Romanowsky 2016; Mackey et al. 2019), which is a factor of 3 more than the number of known GCs in the Milky Way (Harris 1996, 2010). It is not unreasonable to assume that there is also a factor of 3 more, yet to be detected, GC streams in M31 than the ≈ 100 GC streams observed in the Milky Way (Malhan et al. 2018; Mateu 2023; Martin et al. 2022). We know that GCs are also prevalent in other external galaxies (Harris et al. 2013). Thus, M31 and other galaxies could provide a diverse set of GC streams with gaps that can be used to constrain substructure within various frameworks of dark matter (Bovy et al. 2017).

While the full survey parameters of *Roman* is yet to be determined, the proposed high latitude survey (HLS) is expected to image high-latitude fields (Akeson et al. 2019). The WFI instrument can reach depths of ≈ 28 mag (AB) in R, Z, Y bands for exposure times of 1 hour. Furthermore, the instrument has slitless spectroscopic capabilities that cover (0.6 μm -1.8 μm), which will be beneficial in identifying resolved stellar populations, albeit at much shallower 1-hour sensitivity. Compared to previous M31 surveys with HST (e.g. the Panchromatic Hubble Andromeda Treasury Dalcanton et al. 2012), *Roman* will offer an opportunity to observe M31 at higher efficiency and sensitivity.

Finally, in addition to the *Nancy Grace Roman Telescope*, other imaging and astrometric surveys, such as the Vera C. Rubin Observatory, will also help detect new gaps from dark matter subhalos down to $\approx 10^6 M_\odot$ in dozens of streams in the Milky Way (Drlica-Wagner et al. 2019). These detections will offer the possibility to constrain cold dark matter models at a 99 % confidence level, opening up an exciting era for using both Galactic and extra-galactic streams to constrain dark matter models.

6. SUMMARY

Our aim was to quantify the detection prospects of gaps in globular cluster streams in external galaxies with the *Nancy Grace Roman telescope*. To do this, we simulated mock *Roman* observations of gaps in extra-galactic Pal 5-like streams produced by their interaction with dark matter subhalos. We generated mock streams and we simulated a direct encounter with dark matter subhalos with masses between $2 \times 10^6 M_\odot$ and $10^7 M_\odot$. Additionally, we simulated realistic mock observations of background of stars in the halo of M31 at galactocentric radii of 15 kpc, 35 kpc and 55 kpc, taking into account contamination from Milky Way foregrounds. To mimic observations of galaxies at distances that are further than M31, we moved the simulated M31 population to distances of 0.5–10 Mpc, retaining foreground Milky Way populations. To search for gaps in the stream, we first visually inspected mock observations, then applied an analysis with the gap detection tool from Contardo et al. (2022), deriving several metrics to quantify the reliability of our detections with galaxy distance.

We summarize our findings as follows:

- We find that gaps formed by $5 \times 10^6 M_\odot$ subhalos gaps will be visually obvious in 1000 s and 1-hour photometric exposures in the halo of M31.
- Mock observations of the same stream at various distances from the Milky Way indicate that gaps can be seen out to distances of ≈ 1.5 Mpc by visual inspection.
- With the automated detection tool, we confirmed that gaps formed from $5 \times 10^6 M_\odot$ subhalos can be identified to distances of 2–3 Mpc, a volume which includes ≈ 200 galaxies.

While our analysis was limited to gaps from in Pal 5-like streams embedded in M31-like halos, it points to the potential of *Roman* to build a large and diverse set of GC stream gaps in multiple galaxies, which will contribute to constraining various dark matter models.

We thank the CCA dynamics group, Robyn Sanderson, Ivanna Escala, Nora Shipp and the UCSD Coolstars group for insightful discussions. CA thanks Christopher Theissen for providing additional computational resources. This work was developed at the Big Apple Dynamics School in 2021 at the Flatiron Institute. We thank them for their generous support. The Flatiron Institute is supported by the Simons Foundation. This work was made possible through the Preparing for Astrophysics with LSST Program, supported by the Heising-Simons Foundation and managed by Las Cumbres Observatory. Support for SP was provided by NASA through the NASA Hubble Fellowship grant #HST-HF2-51466.001-A awarded by the Space Telescope Science Institute, which is operated by the Association of Universities for Research in Astronomy, Incorporated, under NASA contract NAS5-26555. TS was supported by a CIERA Postdoctoral Fellowship.

Software: Astropy (Price-Whelan et al. 2018), Scipy (Virtanen et al. 2020), Matplotlib (Hunter 2007), Seaborn (Waskom et al. 2014), Numpy (Harris et al. 2020), Pandas (Wes McKinney 2010), Scikit-learn (Pedregosa et al. 2012), FindTheGap (Contardo et al. 2022),

APPENDIX

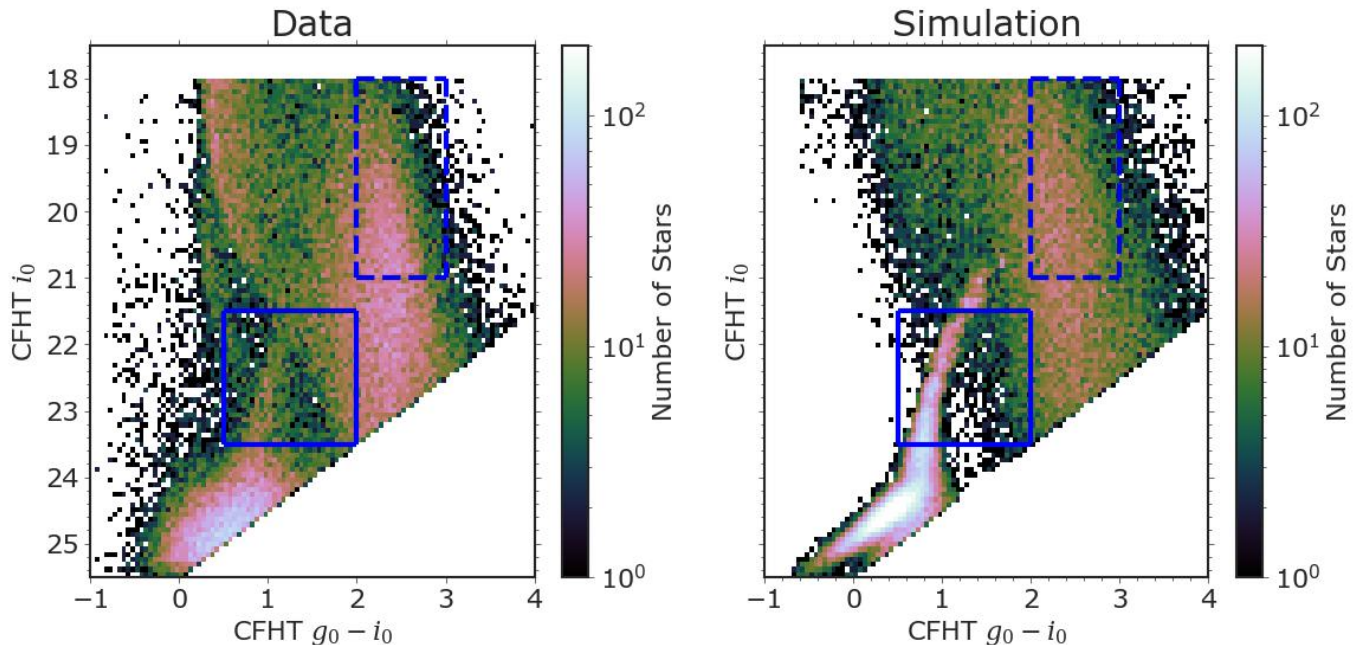


Figure 8. Comparison between simulated stellar populations and the PAndAS data. *Left:* Color-magnitude diagram of the CFHT data from the PAndAS survey covering distances 30–40 kpc from the center of M31. We used the regions shown by the dashed rectangles to scale the number of the Milky Way foreground stars, and the regions shown in solid rectangles to scale the total number of stars in our simulations. *Right:* Similar to the left but here, we show the simulated populations. Our simulated CMD reasonably matches the PAndAS observations.

A. COMPARING SIMULATED POPULATIONS TO PANDAS DATA

In Figure 8, we show the simulated color-magnitude diagram in CFHT g_0 and i_0 bands compared to the reddening-corrected PAndAS data, which reproduces a significant portion of the range of colors and magnitudes covered by the data. We also show the regions of the CMD that were used to scale the simulation to the data. While our simulations are a reasonable match to the data, we did not reproduce overdensities at $g_0 - i_0 \approx 1$ and $i_0 > 22$ which were labeled as Milky Way halo stars by [Ibata et al. \(2014\)](#), pointing to perhaps an underestimation of the fraction of Milky Way disk to halo stars in our simulations. Additionally, our simulations assume magnitude completeness down to the magnitude limits, which is not the case for the real data. As reported by [Martin et al. \(2016\)](#), the completeness of the PAndAS survey drops below 70 percent for $i_0 > 23$. Nevertheless, as discussed in the main text, this scaling provided a robust estimation of the CFHT g -band luminosity function and the total stellar density within the PAndAS fields.

B. ADDITIONAL CHECKS FOR GAP DETECTION PIPELINE

B.1. Visual Inspections of Gap Detections with Distance

Figure 9 shows additional examples of the density of stars in mock observations as a function of distance, and the identification of the gap. Here, we only show streams at $R_{GC} = 35$ kpc and 1 hour exposure time as the gaps are easier to detect (see discussion of Figure 7). The location of the gap is shown by arrows which become scattered beyond 2–3 Mpc, which indicates our detection limit.

B.2. Examples of Non-Detections of Gaps

We demonstrate where the detection of gap breaks down for a set of mock observations $R_{GC} = 35$ kpc and for 1 hour exposure times by showing three cases in Figure 10: (a) a case where the gap was detectable by eye but the bandwidth was much larger than our optimal bandwidth (b) a case where the bandwidth was much smaller than 0.8 kpc, and (c) a case where the bandwidth was optimal but the stellar density in the stream was low. For the first case and second cases, the spread in the location of gap points (\mathcal{S}_g) was large. In the last case, the deviation of gap points (Δ) from the center was large.

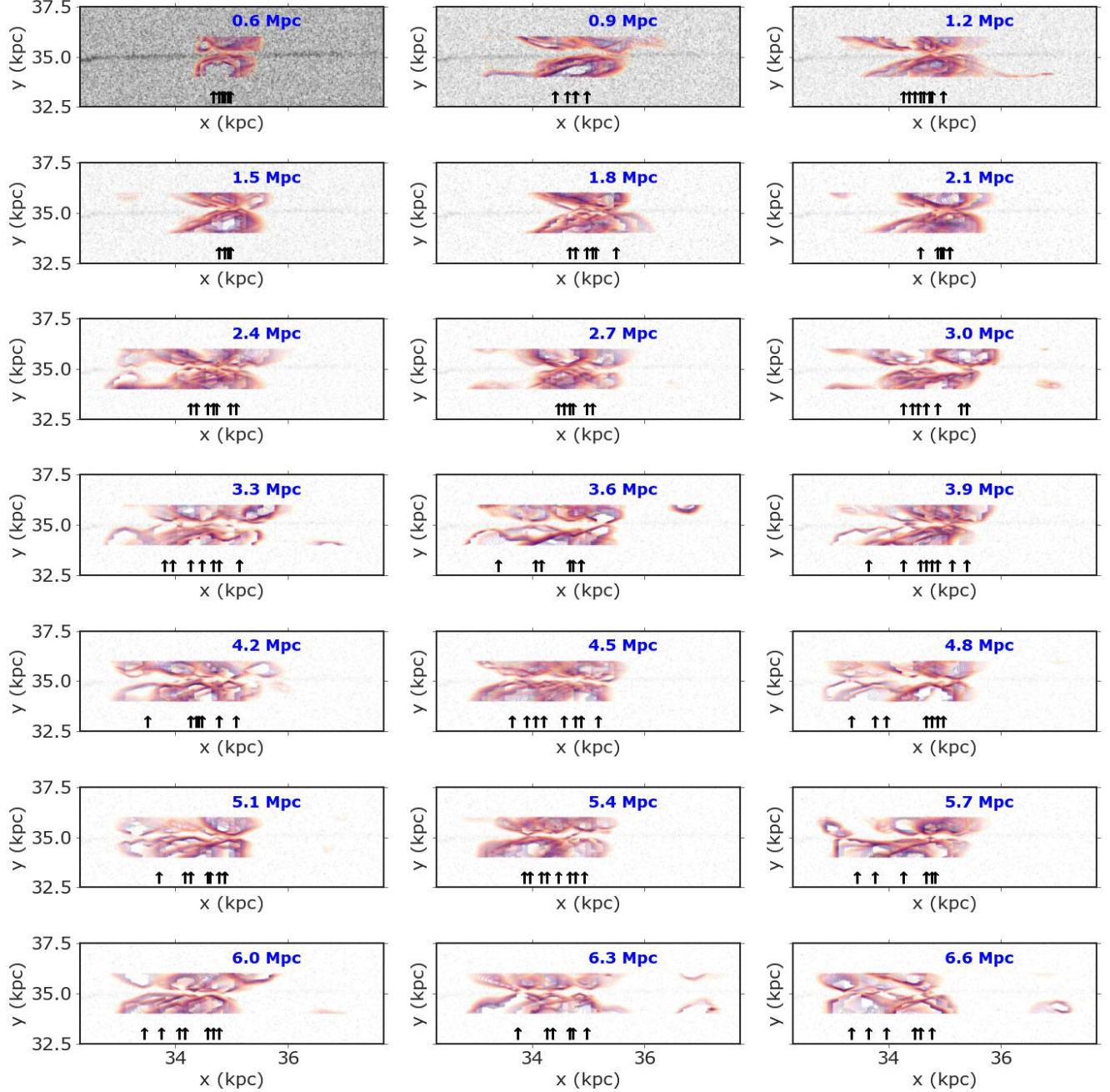


Figure 9. Additional simulation of a gap from a $5 \times 10^6 M_{\odot}$ subhalo at various distances of the host galaxy and for $R_{GC}=35$ kpc. Each panel is a composite of 10 mock observations, and all panels are centered around the gap. Contours show the distribution of the top 95 of the maximum eigenvalues of $\Pi H \Pi$ values based on our density estimator with a bandwidth of 0.8 kpc. Simulated stars are shown as black points. Vertical arrows show the center gap area based on our pipeline for each iteration. Successful identifications of gaps were characterized by a centrally-located gap. Our method successfully identified gaps when the density of stars inside the stream was relatively high (distances $\approx 2-3$ Mpc). We discuss our characterization of potential failure modes of our pipeline in Appendix B.2.

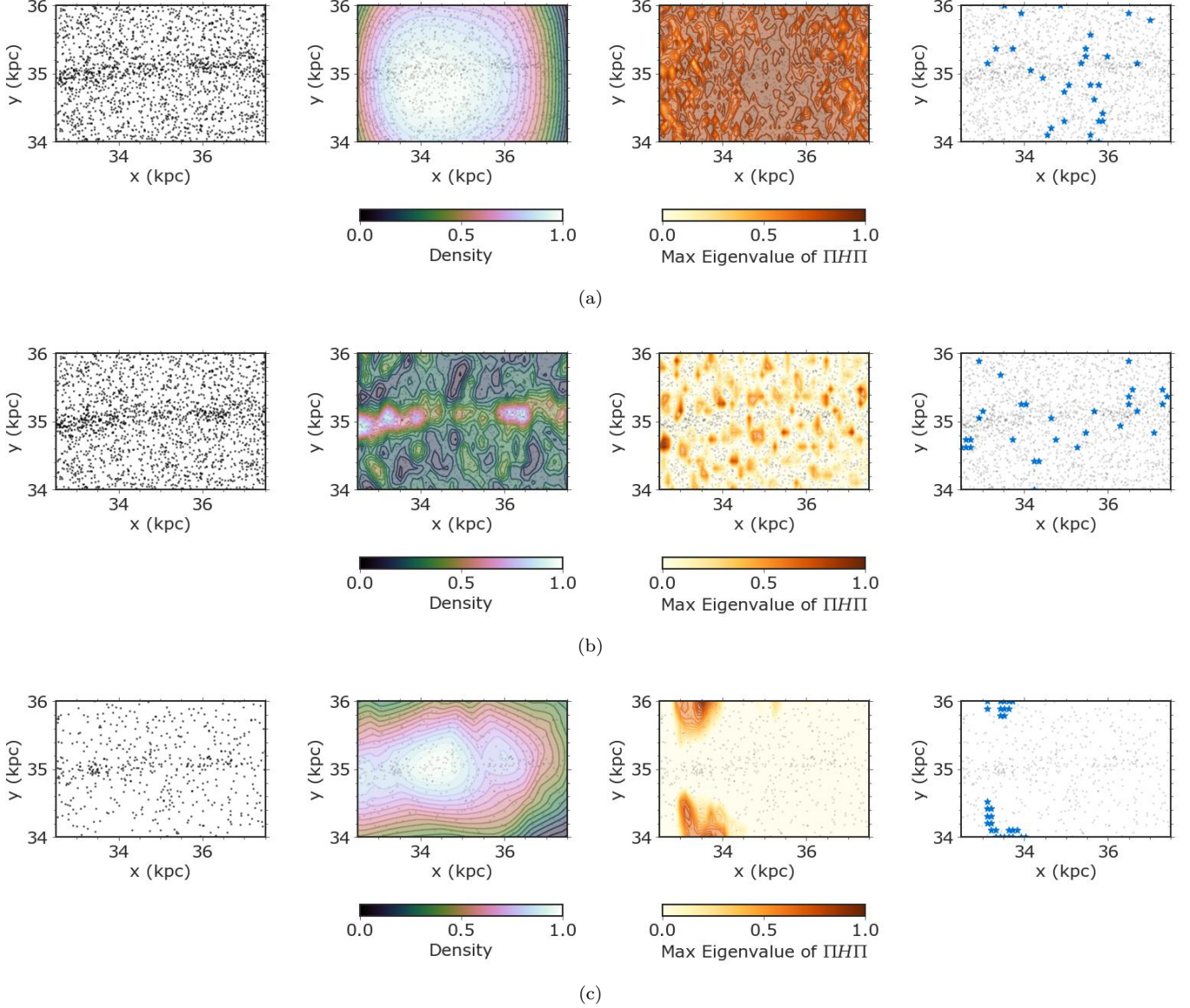


Figure 10. Illustration of different modes of failures for our detection pipeline. All images are for 1 hour exposures. In the left panels, we show the simulations. In the center panels, filled-in contours show the map of the density and the maximum eigenvalues of $\Pi H \Pi$ that we used to locate gaps. In the right panels, we show gap indicator points based on our percentile cuts. (a) Simulation of a stream at a distance of 0.8 Mpc using a large bandwidth of 1.5 kpc. The stream can still be identified, but the method could not detect the central gap. Using our pipeline selection metrics, this detection would be rejected on the basis that the spread in the location of gap points is large and that the absolute deviation of the predicted gap location from the center is large, consistent with our Δ metric (see Section 4.4). (b) Simulation of a stream at a distance of 0.8 Mpc using a bandwidth of 0.1 kpc. In this case, the predicted median location of gap points is close to the true location of the gap, but there are also spurious gaps in the background. Using our metrics defined in Section 4.4, this detection would have a small value for Δ , but a large value for S_g . (c) Simulation of a stream at 6.5 Mpc with a bandwidth of 0.8 kpc. Due to the very low density in the image, the gap-finder tool detects an off-centered gap but it does not detect the real gap. This outcome motivates our claim that the gap detection pipeline works for distances < 3 Mpc.

B.3. Comparing Streams with Gaps to Intact Streams and Backgrounds

We compare the performance of the gap detection tool to simulations of an intact stream with no perturbation from the dark matter subhalo for a bandwidth of 0.5 kpc and 0.8 kpc, and a stream with an off-centered gap with a bandwidth of 0.8 kpc in Figure 11. To generate mock observations, we followed the same methodology as highlighted

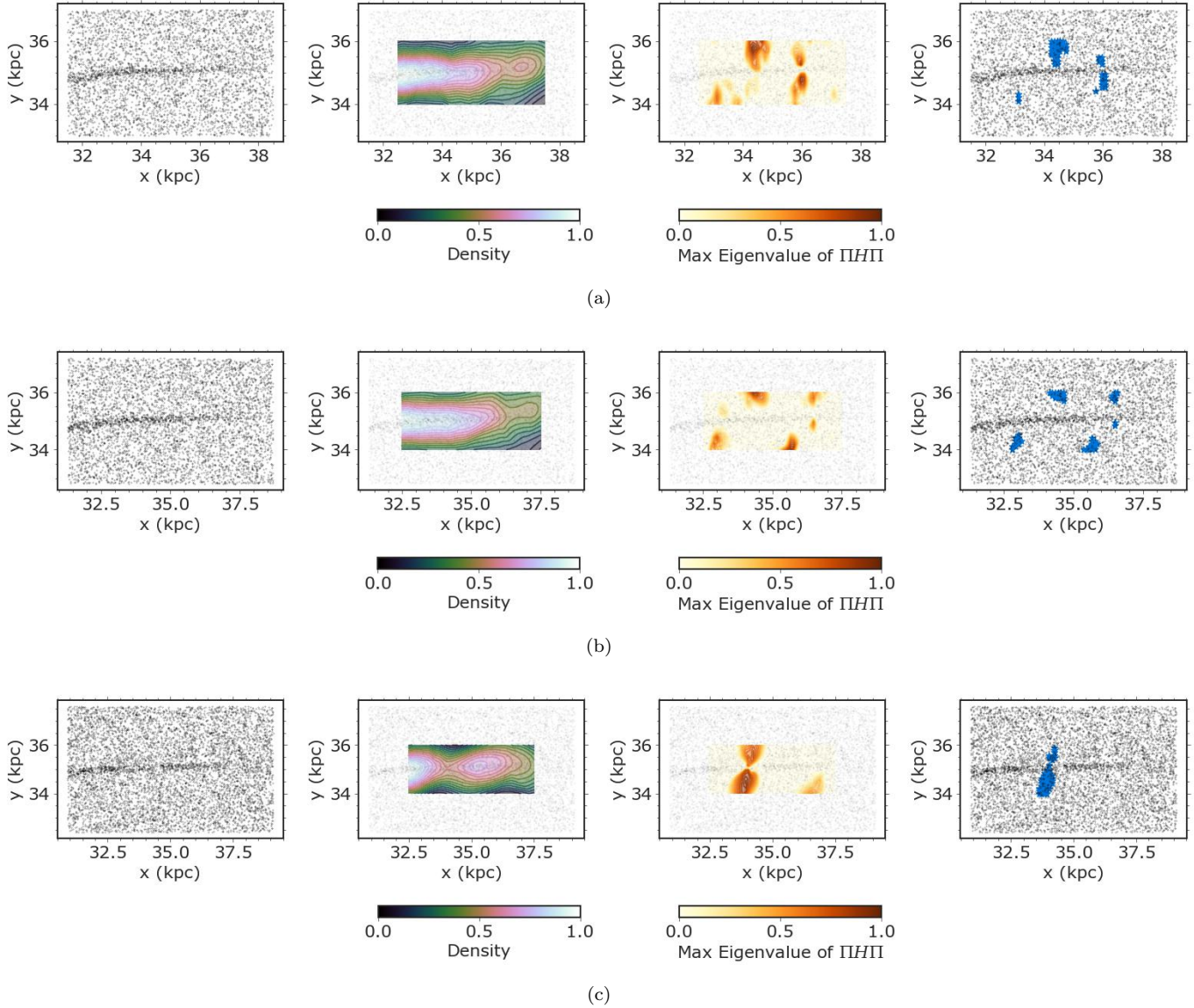


Figure 11. Additional tests of the gap detection tool on intact streams for a bandwidth of 0.5 kpc (a) and a bandwidth of 0.8 kpc (b). We also show a stream with off-centered gap (c), as an additional validation that our pipeline does not depend on the position of the gap. All simulated streams are at 1 Mpc at $R_{GC} = 35$ kpc, for 1000 s exposure.

in the main text. Spurious gaps were persistent in the backgrounds, but these detections can be ruled out by careful visual inspection. Additionally, the tool is able to detect off-centered gaps.

REFERENCES

- Akeson, R., Armus, L., Bachelet, E., et al. 2019, arXiv e-prints, arXiv:1902.05569.
<https://arxiv.org/abs/1902.05569>
- Amara, A., Metcalf, R. B., Cox, T. J., & Ostriker, J. P. 2006, MNRAS, 367, 1367,
 doi: [10.1111/j.1365-2966.2006.10053.x](https://doi.org/10.1111/j.1365-2966.2006.10053.x)
- Amorisco, N. C., Gómez, F. A., Vegetti, S., & White, S. D. M. 2016, MNRAS, 463, L17,
 doi: [10.1093/mnrasl/slw148](https://doi.org/10.1093/mnrasl/slw148)
- Banik, N., & Bovy, J. 2019, MNRAS, 484, 2009,
 doi: [10.1093/mnras/stz142](https://doi.org/10.1093/mnras/stz142)

- Banik, N., Bovy, J., Bertone, G., Erkal, D., & de Boer, T. J. L. 2021, *JCAP*, 2021, 043, doi: [10.1088/1475-7516/2021/10/043](https://doi.org/10.1088/1475-7516/2021/10/043)
- Barry, M., Wetzel, A., Chapman, S., et al. 2023, arXiv e-prints, arXiv:2303.05527. <https://arxiv.org/abs/2303.05527>
- Bechtol, K., Drlica-Wagner, A., Balbinot, E., et al. 2015, *ApJ*, 807, 50, doi: [10.1088/0004-637X/807/1/50](https://doi.org/10.1088/0004-637X/807/1/50)
- Bekki, K., Couch, W. J., Drinkwater, M. J., & Gregg, M. D. 2001, *ApJL*, 557, L39, doi: [10.1086/323075](https://doi.org/10.1086/323075)
- Bhattacharya, S., Arnaboldi, M., Gerhard, O., et al. 2023, arXiv e-prints, arXiv:2305.02761, doi: [10.48550/arXiv.2305.02761](https://doi.org/10.48550/arXiv.2305.02761)
- Blumenthal, G. R., Faber, S. M., Primack, J. R., & Rees, M. J. 1984, *Nature*, 311, 517, doi: [10.1038/311517a0](https://doi.org/10.1038/311517a0)
- Bode, P., Ostriker, J. P., & Turok, N. 2001, *ApJ*, 556, 93, doi: [10.1086/321541](https://doi.org/10.1086/321541)
- Bonaca, A., & Hogg, D. W. 2018, *ApJ*, 867, 101, doi: [10.3847/1538-4357/aae4da](https://doi.org/10.3847/1538-4357/aae4da)
- Bonaca, A., Hogg, D. W., Price-Whelan, A. M., & Conroy, C. 2019, *ApJ*, 880, 38, doi: [10.3847/1538-4357/ab2873](https://doi.org/10.3847/1538-4357/ab2873)
- Bonaca, A., Pearson, S., Price-Whelan, A. M., et al. 2020, *ApJ*, 889, 70, doi: [10.3847/1538-4357/ab5afe](https://doi.org/10.3847/1538-4357/ab5afe)
- Bose, S., Hellwing, W. A., Frenk, C. S., et al. 2017, *MNRAS*, 464, 4520, doi: [10.1093/mnras/stw2686](https://doi.org/10.1093/mnras/stw2686)
- Bovy, J. 2016, *PhRvL*, 116, 121301, doi: [10.1103/PhysRevLett.116.121301](https://doi.org/10.1103/PhysRevLett.116.121301)
- . 2017, *MNRAS*, 470, 1360, doi: [10.1093/mnras/stx1277](https://doi.org/10.1093/mnras/stx1277)
- Bovy, J., Erkal, D., & Sanders, J. L. 2017, *MNRAS*, 466, 628, doi: [10.1093/mnras/stw3067](https://doi.org/10.1093/mnras/stw3067)
- Bovy, J., Allende Prieto, C., Beers, T. C., et al. 2012, *ApJ*, 759, 131, doi: [10.1088/0004-637X/759/2/131](https://doi.org/10.1088/0004-637X/759/2/131)
- Bressan, A., Marigo, P., Girardi, L., et al. 2012, *MNRAS*, 427, 127, doi: [10.1111/j.1365-2966.2012.21948.x](https://doi.org/10.1111/j.1365-2966.2012.21948.x)
- Brown, T. M., Ferguson, H. C., Smith, E., et al. 2003, *ApJL*, 592, L17, doi: [10.1086/376935](https://doi.org/10.1086/376935)
- Bullock, J. S., & Boylan-Kolchin, M. 2017, *ARA&A*, 55, 343, doi: [10.1146/annurev-astro-091916-055313](https://doi.org/10.1146/annurev-astro-091916-055313)
- Bullock, J. S., Kolatt, T. S., Sigad, Y., et al. 2001, *MNRAS*, 321, 559, doi: [10.1046/j.1365-8711.2001.04068.x](https://doi.org/10.1046/j.1365-8711.2001.04068.x)
- Bullock, J. S., Kravtsov, A. V., & Weinberg, D. H. 2000, *ApJ*, 539, 517, doi: [10.1086/309279](https://doi.org/10.1086/309279)
- Caldwell, N., & Romanowsky, A. J. 2016, *ApJ*, 824, 42, doi: [10.3847/0004-637X/824/1/42](https://doi.org/10.3847/0004-637X/824/1/42)
- Carlberg, R. G. 2012, *ApJ*, 748, 20, doi: [10.1088/0004-637X/748/1/20](https://doi.org/10.1088/0004-637X/748/1/20)
- Chamberlain, K., Price-Whelan, A. M., Besla, G., et al. 2022, arXiv e-prints, arXiv:2204.07173. <https://arxiv.org/abs/2204.07173>
- Chapman, S. C., Ibata, R., Lewis, G. F., et al. 2006, *ApJ*, 653, 255, doi: [10.1086/508599](https://doi.org/10.1086/508599)
- Chemin, L., Carignan, C., & Foster, T. 2009, *ApJ*, 705, 1395, doi: [10.1088/0004-637X/705/2/1395](https://doi.org/10.1088/0004-637X/705/2/1395)
- Contardo, G., Hogg, D. W., Hunt, J. A. S., Peek, J. E. G., & Chen, Y.-C. 2022, arXiv e-prints, arXiv:2201.10674. <https://arxiv.org/abs/2201.10674>
- Corbelli, E., Lorenzoni, S., Walterbos, R., Braun, R., & Thilker, D. 2010, *A&A*, 511, A89, doi: [10.1051/0004-6361/200913297](https://doi.org/10.1051/0004-6361/200913297)
- Dalal, N., & Kochanek, C. S. 2002, *ApJ*, 572, 25, doi: [10.1086/340303](https://doi.org/10.1086/340303)
- Dalcanton, J. J., Williams, B. F., Lang, D., et al. 2012, *ApJS*, 200, 18, doi: [10.1088/0067-0049/200/2/18](https://doi.org/10.1088/0067-0049/200/2/18)
- Dalcanton, J. J., Fouesneau, M., Hogg, D. W., et al. 2015, *ApJ*, 814, 3, doi: [10.1088/0004-637X/814/1/3](https://doi.org/10.1088/0004-637X/814/1/3)
- de Boer, T. J. L., Belokurov, V., Koposov, S. E., et al. 2018, *MNRAS*, 477, 1893, doi: [10.1093/mnras/sty677](https://doi.org/10.1093/mnras/sty677)
- de Boer, T. J. L., Erkal, D., & Gieles, M. 2020, *MNRAS*, 494, 5315, doi: [10.1093/mnras/staa917](https://doi.org/10.1093/mnras/staa917)
- Dey, A., Najita, J. R., Koposov, S. E., et al. 2022, arXiv e-prints, arXiv:2208.11683, doi: [10.48550/arXiv.2208.11683](https://doi.org/10.48550/arXiv.2208.11683)
- Doke, Y., & Hattori, K. 2022, arXiv e-prints, arXiv:2203.15481. <https://arxiv.org/abs/2203.15481>
- Drlica-Wagner, A., Bechtol, K., Rykoff, E. S., et al. 2015, *ApJ*, 813, 109, doi: [10.1088/0004-637X/813/2/109](https://doi.org/10.1088/0004-637X/813/2/109)
- Drlica-Wagner, A., Mao, Y.-Y., Adhikari, S., et al. 2019, arXiv e-prints, arXiv:1902.01055. <https://arxiv.org/abs/1902.01055>
- D'Souza, R., & Bell, E. F. 2018, *Nature Astronomy*, 2, 737, doi: [10.1038/s41550-018-0533-x](https://doi.org/10.1038/s41550-018-0533-x) [10.48550/arXiv.1807.08819](https://doi.org/10.48550/arXiv.1807.08819)
- Efstathiou, G. 1992, *MNRAS*, 256, 43P, doi: [10.1093/mnras/256.1.43P](https://doi.org/10.1093/mnras/256.1.43P)
- Erkal, D., & Belokurov, V. 2015, *MNRAS*, 450, 1136, doi: [10.1093/mnras/stv655](https://doi.org/10.1093/mnras/stv655)
- Erkal, D., Belokurov, V., Bovy, J., & Sanders, J. L. 2016, *MNRAS*, 463, 102, doi: [10.1093/mnras/stw1957](https://doi.org/10.1093/mnras/stw1957)
- Erkal, D., Koposov, S. E., & Belokurov, V. 2017, *MNRAS*, 470, 60, doi: [10.1093/mnras/stx1208](https://doi.org/10.1093/mnras/stx1208)
- Erkal, D., Belokurov, V., Laporte, C. F. P., et al. 2019, *MNRAS*, 487, 2685, doi: [10.1093/mnras/stz1371](https://doi.org/10.1093/mnras/stz1371)
- Errani, R., & Peñarrubia, J. 2020, *MNRAS*, 491, 4591, doi: [10.1093/mnras/stz3349](https://doi.org/10.1093/mnras/stz3349)
- Escala, I., Gilbert, K. M., Kirby, E. N., et al. 2020, *ApJ*, 889, 177, doi: [10.3847/1538-4357/ab6659](https://doi.org/10.3847/1538-4357/ab6659)
- Escala, I., Gilbert, K. M., Wojno, J., Kirby, E. N., & Guhathakurta, P. 2021, *AJ*, 162, 45, doi: [10.3847/1538-3881/abfec410](https://doi.org/10.3847/1538-3881/abfec410) [10.48550/arXiv.2105.02339](https://doi.org/10.48550/arXiv.2105.02339)

- Fardal, M. A., Huang, S., & Weinberg, M. D. 2015, *MNRAS*, 452, 301, doi: [10.1093/mnras/stv1198](https://doi.org/10.1093/mnras/stv1198)
- Fardal, M. A., Weinberg, M. D., Babul, A., et al. 2013, *MNRAS*, 434, 2779, doi: [10.1093/mnras/stt1121](https://doi.org/10.1093/mnras/stt1121)
- Fiacconi, D., Madau, P., Potter, D., & Stadel, J. 2016, *ApJ*, 824, 144, doi: [10.3847/0004-637X/824/2/144](https://doi.org/10.3847/0004-637X/824/2/144)
- Font, A. S., Johnston, K. V., Guhathakurta, P., Majewski, S. R., & Rich, R. M. 2006, *AJ*, 131, 1436, doi: [10.1086/499564](https://doi.org/10.1086/499564)
- Forouhar Moreno, V. J., Benítez-Llambay, A., Cole, S., & Frenk, C. 2022, *MNRAS*, 517, 5627, doi: [10.1093/mnras/stac3062](https://doi.org/10.1093/mnras/stac3062)
- Galleti, S., Bellazzini, M., Federici, L., Buzzoni, A., & Fusi Pecci, F. 2007, *A&A*, 471, 127, doi: [10.1051/0004-6361:20077788](https://doi.org/10.1051/0004-6361:20077788)
- Galleti, S., Federici, L., Bellazzini, M., Buzzoni, A., & Fusi Pecci, F. 2006, *A&A*, 456, 985, doi: [10.1051/0004-6361:20065309](https://doi.org/10.1051/0004-6361:20065309)
- Garavito-Camargo, N., Besla, G., Laporte, C. F. P., et al. 2019, *ApJ*, 884, 51, doi: [10.3847/1538-4357/ab32eb](https://doi.org/10.3847/1538-4357/ab32eb)
- Garrison-Kimmel, S., Wetzel, A., Bullock, J. S., et al. 2017, *MNRAS*, 471, 1709, doi: [10.1093/mnras/stx1710](https://doi.org/10.1093/mnras/stx1710)
- Geehan, J. J., Fardal, M. A., Babul, A., & Guhathakurta, P. 2006, *MNRAS*, 366, 996, doi: [10.1111/j.1365-2966.2005.09863.x](https://doi.org/10.1111/j.1365-2966.2005.09863.x)
- Geha, M., Wechsler, R. H., Mao, Y.-Y., et al. 2017, *ApJ*, 847, 4, doi: [10.3847/1538-4357/aa8626](https://doi.org/10.3847/1538-4357/aa8626)
- Gilman, D., Birrer, S., Treu, T., Nierenberg, A., & Benson, A. 2019, *MNRAS*, 487, 5721, doi: [10.1093/mnras/stz1593](https://doi.org/10.1093/mnras/stz1593)
- Glennon, N., Nadler, E. O., Musoke, N., et al. 2022, *PhRvD*, 105, 123540, doi: [10.1103/PhysRevD.105.123540](https://doi.org/10.1103/PhysRevD.105.123540)
- González, R. E., Kravtsov, A. V., & Gnedin, N. Y. 2014, *ApJ*, 793, 91, doi: [10.1088/0004-637X/793/2/91](https://doi.org/10.1088/0004-637X/793/2/91)
- GRAVITY Collaboration, Abuter, R., Amorim, A., et al. 2019, *A&A*, 625, L10, doi: [10.1051/0004-6361/201935656](https://doi.org/10.1051/0004-6361/201935656)
- Grillmair, C. J., & Carlin, J. L. 2016, in *Astrophysics and Space Science Library*, Vol. 420, *Tidal Streams in the Local Group and Beyond*, ed. H. J. Newberg & J. L. Carlin, 87, doi: [10.1007/978-3-319-19336-6_4](https://doi.org/10.1007/978-3-319-19336-6_4)
- Grillmair, C. J., & Smith, G. H. 2001, *AJ*, 122, 3231, doi: [10.1086/323916](https://doi.org/10.1086/323916)
- Harris, C. R., Millman, K. J., van der Walt, S. J., et al. 2020, *Nature*, 585, 357, doi: [10.1038/s41586-020-2649-2](https://doi.org/10.1038/s41586-020-2649-2)
- Harris, W. E. 1996, *AJ*, 112, 1487, doi: [10.1086/118116](https://doi.org/10.1086/118116)
- . 2010, arXiv e-prints, arXiv:1012.3224. <https://arxiv.org/abs/1012.3224>
- Harris, W. E., Harris, G. L. H., & Alessi, M. 2013, *ApJ*, 772, 82, doi: [10.1088/0004-637X/772/2/82](https://doi.org/10.1088/0004-637X/772/2/82)
- Hattori, K., Erkal, D., & Sanders, J. L. 2016, *MNRAS*, 460, 497, doi: [10.1093/mnras/stw1006](https://doi.org/10.1093/mnras/stw1006)
- Hawkins, K., Jofré, P., Masseron, T., & Gilmore, G. 2015, *MNRAS*, 453, 758, doi: [10.1093/mnras/stv1586](https://doi.org/10.1093/mnras/stv1586)
- Helmi, A., & White, S. D. M. 1999, *MNRAS*, 307, 495, doi: [10.1046/j.1365-8711.1999.02616.x](https://doi.org/10.1046/j.1365-8711.1999.02616.x)
- Hendel, D., Johnston, K. V., Patra, R. K., & Sen, B. 2019, *MNRAS*, 486, 3604, doi: [10.1093/mnras/stz1107](https://doi.org/10.1093/mnras/stz1107)
- Hermans, J., Banik, N., Weniger, C., Bertone, G., & Louppe, G. 2021, *MNRAS*, 507, 1999, doi: [10.1093/mnras/stab2181](https://doi.org/10.1093/mnras/stab2181)
- Hernquist, L. 1990, *ApJ*, 356, 359, doi: [10.1086/168845](https://doi.org/10.1086/168845)
- Hezaveh, Y., Dalal, N., Holder, G., et al. 2016, *JCAP*, 2016, 048, doi: [10.1088/1475-7516/2016/11/048](https://doi.org/10.1088/1475-7516/2016/11/048)
- Hu, W., Barkana, R., & Gruzinov, A. 2000, *PhRvL*, 85, 1158, doi: [10.1103/PhysRevLett.85.1158](https://doi.org/10.1103/PhysRevLett.85.1158)
- Hui, L., Ostriker, J. P., Tremaine, S., & Witten, E. 2017, *PhRvD*, 95, 043541, doi: [10.1103/PhysRevD.95.043541](https://doi.org/10.1103/PhysRevD.95.043541)
- Hunter, J. D. 2007, *Computing in Science Engineering*, 9, 90, doi: [10.1109/MCSE.2007.55](https://doi.org/10.1109/MCSE.2007.55)
- Huxor, A. P., Tanvir, N. R., Ferguson, A. M. N., et al. 2008, *MNRAS*, 385, 1989, doi: [10.1111/j.1365-2966.2008.12882.x](https://doi.org/10.1111/j.1365-2966.2008.12882.x)
- Huxor, A. P., Mackey, A. D., Ferguson, A. M. N., et al. 2014, *MNRAS*, 442, 2165, doi: [10.1093/mnras/stu771](https://doi.org/10.1093/mnras/stu771)
- Ibata, R. A., Lewis, G. F., Thomas, G., Martin, N. F., & Chapman, S. 2017, *ApJ*, 842, 120, doi: [10.3847/1538-4357/aa7514](https://doi.org/10.3847/1538-4357/aa7514)
- Ibata, R. A., Malhan, K., & Martin, N. F. 2019, *ApJ*, 872, 152, doi: [10.3847/1538-4357/ab0080](https://doi.org/10.3847/1538-4357/ab0080)
- Ibata, R. A., Lewis, G. F., McConnachie, A. W., et al. 2014, *ApJ*, 780, 128, doi: [10.1088/0004-637X/780/2/128](https://doi.org/10.1088/0004-637X/780/2/128)
- Jofré, P., & Weiss, A. 2011, *A&A*, 533, A59, doi: [10.1051/0004-6361/201117131](https://doi.org/10.1051/0004-6361/201117131)
- Johnston, K. V. 1998, *ApJ*, 495, 297, doi: [10.1086/305273](https://doi.org/10.1086/305273)
- Johnston, K. V., Spergel, D. N., & Haydn, C. 2002, *ApJ*, 570, 656, doi: [10.1086/339791](https://doi.org/10.1086/339791)
- Jurić, M., Ivezić, Ž., Brooks, A., et al. 2008, *ApJ*, 673, 864, doi: [10.1086/523619](https://doi.org/10.1086/523619)
- Kafle, P. R., Sharma, S., Lewis, G. F., Robotham, A. S. G., & Driver, S. P. 2018, *MNRAS*, 475, 4043, doi: [10.1093/mnras/sty082](https://doi.org/10.1093/mnras/sty082)
- Karachentsev, I. D., & Kaisina, E. I. 2019, *Astrophysical Bulletin*, 74, 111, doi: [10.1134/S1990341319020019](https://doi.org/10.1134/S1990341319020019)
- Kilic, M., Munn, J. A., Harris, H. C., et al. 2017, *ApJ*, 837, 162, doi: [10.3847/1538-4357/aa62a5](https://doi.org/10.3847/1538-4357/aa62a5)
- Koposov, S. E., Yoo, J., Rix, H.-W., et al. 2009, *ApJ*, 696, 2179, doi: [10.1088/0004-637X/696/2/2179](https://doi.org/10.1088/0004-637X/696/2/2179)
- Koppelman, H. H., & Helmi, A. 2021, *A&A*, 649, A55, doi: [10.1051/0004-6361/202039968](https://doi.org/10.1051/0004-6361/202039968)
- Kroupa, P. 2001, *MNRAS*, 322, 231, doi: [10.1046/j.1365-8711.2001.04022.x](https://doi.org/10.1046/j.1365-8711.2001.04022.x)

- Kruijssen, J. M. D., Pfeffer, J. L., Chevance, M., et al. 2020, *MNRAS*, 498, 2472, doi: [10.1093/mnras/staa2452](https://doi.org/10.1093/mnras/staa2452)
- Li, T. S., Ji, A. P., Pace, A. B., et al. 2022, *ApJ*, 928, 30, doi: [10.3847/1538-4357/ac46d3](https://doi.org/10.3847/1538-4357/ac46d3)
- Lilleengen, S., Petersen, M. S., Erkal, D., et al. 2023, *MNRAS*, 518, 774, doi: [10.1093/mnras/stac3108](https://doi.org/10.1093/mnras/stac3108)
- Liu, C., Xu, Y., Wan, J.-C., et al. 2017, *Research in Astronomy and Astrophysics*, 17, 096, doi: [10.1088/1674-4527/17/9/96](https://doi.org/10.1088/1674-4527/17/9/96)
- Lovell, M. R., Cautun, M., Frenk, C. S., Hellwing, W. A., & Newton, O. 2021, *MNRAS*, 507, 4826, doi: [10.1093/mnras/stab2452](https://doi.org/10.1093/mnras/stab2452)
- Mackereth, J. T., Schiavon, R. P., Pfeffer, J., et al. 2019, *MNRAS*, 482, 3426, doi: [10.1093/mnras/sty2955](https://doi.org/10.1093/mnras/sty2955)
- Mackey, A. D., Ferguson, A. M. N., Huxor, A. P., et al. 2019, *MNRAS*, 484, 1756, doi: [10.1093/mnras/stz072](https://doi.org/10.1093/mnras/stz072)
- Majewski, S. R., Skrutskie, M. F., Weinberg, M. D., & Ostheimer, J. C. 2003, *ApJ*, 599, 1082, doi: [10.1086/379504](https://doi.org/10.1086/379504)
- Malhan, K., & Ibata, R. A. 2018, *MNRAS*, 477, 4063, doi: [10.1093/mnras/sty912](https://doi.org/10.1093/mnras/sty912)
- Malhan, K., Ibata, R. A., & Martin, N. F. 2018, *MNRAS*, 481, 3442, doi: [10.1093/mnras/sty2474](https://doi.org/10.1093/mnras/sty2474)
- Mao, Y.-Y., Geha, M., Wechsler, R. H., et al. 2021, *ApJ*, 907, 85, doi: [10.3847/1538-4357/abce58](https://doi.org/10.3847/1538-4357/abce58)
- Martin, N. F., de Jong, J. T. A., & Rix, H.-W. 2008, *ApJ*, 684, 1075, doi: [10.1086/590336](https://doi.org/10.1086/590336)
- Martin, N. F., Ibata, R. A., Lewis, G. F., et al. 2016, *ApJ*, 833, 167, doi: [10.3847/1538-4357/833/2/167](https://doi.org/10.3847/1538-4357/833/2/167)
- Martin, N. F., Ibata, R. A., Starkenburg, E., et al. 2022, *MNRAS*, 516, 5331, doi: [10.1093/mnras/stac2426](https://doi.org/10.1093/mnras/stac2426)
- Martínez-Delgado, D., Gabany, R. J., Crawford, K., et al. 2010, *AJ*, 140, 962, doi: [10.1088/0004-6256/140/4/962](https://doi.org/10.1088/0004-6256/140/4/962)
- Martinez-Delgado, D., Cooper, A. P., Roman, J., et al. 2021, arXiv e-prints, arXiv:2104.06071. <https://arxiv.org/abs/2104.06071>
- Mateu, C. 2023, *MNRAS*, doi: [10.1093/mnras/stad321](https://doi.org/10.1093/mnras/stad321)
- Mateu, C., Cooper, A. P., Font, A. S., et al. 2017, *MNRAS*, 469, 721, doi: [10.1093/mnras/stx872](https://doi.org/10.1093/mnras/stx872)
- Mateu, C., Read, J. I., & Kawata, D. 2018, *MNRAS*, 474, 4112, doi: [10.1093/mnras/stx2937](https://doi.org/10.1093/mnras/stx2937)
- McConnachie, A. W. 2012, *AJ*, 144, 4, doi: [10.1088/0004-6256/144/1/4](https://doi.org/10.1088/0004-6256/144/1/4)
- McConnachie, A. W., Irwin, M. J., Ibata, R. A., et al. 2009, *Nature*, 461, 66, doi: [10.1038/nature08327](https://doi.org/10.1038/nature08327)
- McConnachie, A. W., Ibata, R., Martin, N., et al. 2018, *ApJ*, 868, 55, doi: [10.3847/1538-4357/aae8e7](https://doi.org/10.3847/1538-4357/aae8e7)
- McMillan, P. J. 2017, *MNRAS*, 465, 76, doi: [10.1093/mnras/stw2759](https://doi.org/10.1093/mnras/stw2759)
- Miyamoto, M., & Nagai, R. 1975, *PASJ*, 27, 533
- Navarro, J. F., Eke, V. R., & Frenk, C. S. 1996, *MNRAS*, 283, L72, doi: [10.1093/mnras/283.3.L72](https://doi.org/10.1093/mnras/283.3.L72)
- Newberg, H. J., Yanny, B., & Willett, B. A. 2009, *ApJL*, 700, L61, doi: [10.1088/0004-637X/700/2/L61](https://doi.org/10.1088/0004-637X/700/2/L61)
- Newberg, H. J., Yanny, B., Rockosi, C., et al. 2002, *ApJ*, 569, 245, doi: [10.1086/338983](https://doi.org/10.1086/338983)
- Nierenberg, A. M., Treu, T., Wright, S. A., Fassnacht, C. D., & Auger, M. W. 2014, *MNRAS*, 442, 2434, doi: [10.1093/mnras/stu862](https://doi.org/10.1093/mnras/stu862)
- Nierenberg, A. M., Treu, T., Brammer, G., et al. 2017, *MNRAS*, 471, 2224, doi: [10.1093/mnras/stx1400](https://doi.org/10.1093/mnras/stx1400)
- Nitschai, M. S., Eilers, A.-C., Neumayer, N., Cappellari, M., & Rix, H.-W. 2021, *ApJ*, 916, 112, doi: [10.3847/1538-4357/ac04b5](https://doi.org/10.3847/1538-4357/ac04b5)
- Odenkirchen, M., Grebel, E. K., Kayser, A., Rix, H.-W., & Dehnen, W. 2009, *AJ*, 137, 3378, doi: [10.1088/0004-6256/137/2/3378](https://doi.org/10.1088/0004-6256/137/2/3378)
- Odenkirchen, M., Grebel, E. K., Rockosi, C. M., et al. 2001, *ApJL*, 548, L165, doi: [10.1086/319095](https://doi.org/10.1086/319095)
- Odenkirchen, M., Grebel, E. K., Dehnen, W., et al. 2003, *AJ*, 126, 2385, doi: [10.1086/378601](https://doi.org/10.1086/378601)
- Okamoto, T., Gao, L., & Theuns, T. 2008, *MNRAS*, 390, 920, doi: [10.1111/j.1365-2966.2008.13830.x](https://doi.org/10.1111/j.1365-2966.2008.13830.x)
- Peñarrubia, J., Walker, M. G., & Gilmore, G. 2009, *MNRAS*, 399, 1275, doi: [10.1111/j.1365-2966.2009.15027.x](https://doi.org/10.1111/j.1365-2966.2009.15027.x)
- Pearson, S., Clark, S. E., Demirjian, A. J., et al. 2022, *ApJ*, 926, 166, doi: [10.3847/1538-4357/ac4496](https://doi.org/10.3847/1538-4357/ac4496)
- Pearson, S., Price-Whelan, A. M., & Johnston, K. V. 2017, *Nature Astronomy*, 1, 633, doi: [10.1038/s41550-017-0220-3](https://doi.org/10.1038/s41550-017-0220-3)
- Pearson, S., Starkenburg, T. K., Johnston, K. V., et al. 2019, *ApJ*, 883, 87, doi: [10.3847/1538-4357/ab3e06](https://doi.org/10.3847/1538-4357/ab3e06)
- Pedregosa, F., Varoquaux, G., Gramfort, A., et al. 2012, arXiv e-prints, arXiv:1201.0490. <https://arxiv.org/abs/1201.0490>
- Planck Collaboration, Aghanim, N., Akrami, Y., et al. 2020, *A&A*, 641, A6, doi: [10.1051/0004-6361/201833910](https://doi.org/10.1051/0004-6361/201833910)
- Price-Whelan, A. M. 2017, *The Journal of Open Source Software*, 2, doi: [10.21105/joss.00388](https://doi.org/10.21105/joss.00388)
- Price-Whelan, A. M., & Bonaca, A. 2018, *ApJL*, 863, L20, doi: [10.3847/2041-8213/aad7b5](https://doi.org/10.3847/2041-8213/aad7b5)
- Price-Whelan, A. M., Johnston, K. V., Valluri, M., et al. 2016, *MNRAS*, 455, 1079, doi: [10.1093/mnras/stv2383](https://doi.org/10.1093/mnras/stv2383)
- Price-Whelan, A. M., Mateu, C., Iorio, G., et al. 2019, *AJ*, 158, 223, doi: [10.3847/1538-3881/ab4cef](https://doi.org/10.3847/1538-3881/ab4cef)
- Price-Whelan, A. M., Sipőcz, B. M., Günther, H. M., et al. 2018, *AJ*, 156, 123, doi: [10.3847/1538-3881/aabc4f](https://doi.org/10.3847/1538-3881/aabc4f)
- Reylé, C., Marshall, D. J., Robin, A. C., & Schultheis, M. 2009, *A&A*, 495, 819, doi: [10.1051/0004-6361/200811341](https://doi.org/10.1051/0004-6361/200811341)

- Rocha, M., Peter, A. H. G., Bullock, J. S., et al. 2013, MNRAS, 430, 81, doi: [10.1093/mnras/sts514](https://doi.org/10.1093/mnras/sts514)
- Sanders, J. L., Bovy, J., & Erkal, D. 2016, MNRAS, 457, 3817, doi: [10.1093/mnras/stw232](https://doi.org/10.1093/mnras/stw232)
- Sanderson, R. E., Vera-Ciro, C., Helmi, A., & Heit, J. 2016, arXiv e-prints, arXiv:1608.05624, doi: [10.48550/arXiv.1608.05624](https://doi.org/10.48550/arXiv.1608.05624)
- Sawala, T., Frenk, C. S., Fattahi, A., et al. 2016, MNRAS, 456, 85, doi: [10.1093/mnras/stv2597](https://doi.org/10.1093/mnras/stv2597)
- Schönrich, R., Binney, J., & Dehnen, W. 2010, MNRAS, 403, 1829, doi: [10.1111/j.1365-2966.2010.16253.x](https://doi.org/10.1111/j.1365-2966.2010.16253.x)
- Seigar, M. S., Barth, A. J., & Bullock, J. S. 2008, MNRAS, 389, 1911, doi: [10.1111/j.1365-2966.2008.13732.x](https://doi.org/10.1111/j.1365-2966.2008.13732.x)
- Shih, D., Buckley, M. R., & Necib, L. 2023, arXiv e-prints, arXiv:2303.01529, doi: [10.48550/arXiv.2303.01529](https://doi.org/10.48550/arXiv.2303.01529)
- Shih, D., Buckley, M. R., Necib, L., & Tamasas, J. 2022, MNRAS, 509, 5992, doi: [10.1093/mnras/stab3372](https://doi.org/10.1093/mnras/stab3372)
- Shipp, N., Drlica-Wagner, A., Balbinot, E., et al. 2018, ApJ, 862, 114, doi: [10.3847/1538-4357/aacdab](https://doi.org/10.3847/1538-4357/aacdab)
- Shipp, N., Erkal, D., Drlica-Wagner, A., et al. 2021, ApJ, 923, 149, doi: [10.3847/1538-4357/ac2e93](https://doi.org/10.3847/1538-4357/ac2e93)
- Simon, J. D., & Geha, M. 2007, ApJ, 670, 313, doi: [10.1086/521816](https://doi.org/10.1086/521816)
- Spergel, D., Gehrels, N., Baltay, C., et al. 2015, arXiv e-prints, arXiv:1503.03757. <https://arxiv.org/abs/1503.03757>
- Spergel, D. N., & Steinhardt, P. J. 2000, PhRvL, 84, 3760, doi: [10.1103/PhysRevLett.84.3760](https://doi.org/10.1103/PhysRevLett.84.3760)
- Springel, V., Wang, J., Vogelsberger, M., et al. 2008, MNRAS, 391, 1685, doi: [10.1111/j.1365-2966.2008.14066.x](https://doi.org/10.1111/j.1365-2966.2008.14066.x)
- Tamm, A., Tempel, E., Tenjes, P., Tihhonova, O., & Tuvikene, T. 2012, A&A, 546, A4, doi: [10.1051/0004-6361/201220065](https://doi.org/10.1051/0004-6361/201220065)
- Tavangar, K., Ferguson, P., Shipp, N., et al. 2022, ApJ, 925, 118, doi: [10.3847/1538-4357/ac399b](https://doi.org/10.3847/1538-4357/ac399b)
- Tulin, S., & Yu, H.-B. 2018, PhR, 730, 1, doi: [10.1016/j.physrep.2017.11.004](https://doi.org/10.1016/j.physrep.2017.11.004)
- van den Bosch, F. C., & Ogiya, G. 2018, MNRAS, 475, 4066, doi: [10.1093/mnras/sty084](https://doi.org/10.1093/mnras/sty084)
- van den Bosch, F. C., Ogiya, G., Hahn, O., & Burkert, A. 2018, MNRAS, 474, 3043, doi: [10.1093/mnras/stx2956](https://doi.org/10.1093/mnras/stx2956)
- Vasiliev, E. 2019, MNRAS, 484, 2832, doi: [10.1093/mnras/stz171](https://doi.org/10.1093/mnras/stz171)
- Virtanen, P., Gommers, R., et al. 2020, Nature Methods, 17, 261, doi: [10.1038/s41592-019-0686-2](https://doi.org/10.1038/s41592-019-0686-2)
- Waskom, M., Botvinnik, O., Hobson, P., et al. 2014, seaborn: v0.5.0 (November 2014), v0.5.0, Zenodo, doi: [10.5281/zenodo.12710](https://doi.org/10.5281/zenodo.12710)
- Watkins, L. L., Evans, N. W., & An, J. H. 2010, MNRAS, 406, 264, doi: [10.1111/j.1365-2966.2010.16708.x](https://doi.org/10.1111/j.1365-2966.2010.16708.x)
- Weinberg, M. D. 1998, MNRAS, 299, 499, doi: [10.1046/j.1365-8711.1998.01790.x](https://doi.org/10.1046/j.1365-8711.1998.01790.x)
- Wes McKinney. 2010, in Proceedings of the 9th Python in Science Conference, ed. Stéfan van der Walt & Jarrod Millman, 56 – 61, doi: [10.25080/Majora-92bf1922-00a](https://doi.org/10.25080/Majora-92bf1922-00a)
- White, S. D. M., & Rees, M. J. 1978, MNRAS, 183, 341, doi: [10.1093/mnras/183.3.341](https://doi.org/10.1093/mnras/183.3.341)
- Willman, B., Geha, M., Strader, J., et al. 2011, AJ, 142, 128, doi: [10.1088/0004-6256/142/4/128](https://doi.org/10.1088/0004-6256/142/4/128)
- Willman, B., Blanton, M. R., West, A. A., et al. 2005, AJ, 129, 2692, doi: [10.1086/430214](https://doi.org/10.1086/430214)
- Yoon, J. H., Johnston, K. V., & Hogg, D. W. 2011, ApJ, 731, 58, doi: [10.1088/0004-637X/731/1/58](https://doi.org/10.1088/0004-637X/731/1/58)